



# European NO<sub>x</sub> emissions in WRF-Chem derived from OMI: impacts on summertime surface ozone

Auke J. Visser<sup>1</sup>, K. Folkert Boersma<sup>1,2</sup>, Laurens N. Ganzeveld<sup>1</sup>, and Maarten C. Krol<sup>1,3</sup>

<sup>1</sup>Wageningen University, Meteorology and Air Quality Section, Wageningen, the Netherlands

<sup>2</sup>Royal Netherlands Meteorological Institute, R&D Satellite Observations, de Bilt, the Netherlands

<sup>3</sup>Utrecht University, Institute for Marine and Atmospheric Research Utrecht, Utrecht, the Netherlands

**Correspondence:** Auke J. Visser (auke.visser@wur.nl)

Received: 27 March 2019 – Discussion started: 29 April 2019

Revised: 27 August 2019 – Accepted: 28 August 2019 – Published: 24 September 2019

**Abstract.** Ozone (O<sub>3</sub>) is a secondary air pollutant that negatively affects human and ecosystem health. Ozone simulations with regional air quality models suffer from unexplained biases over Europe, and uncertainties in the emissions of ozone precursor group nitrogen oxides (NO<sub>x</sub> = NO + NO<sub>2</sub>) contribute to these biases. The goal of this study is to use NO<sub>2</sub> column observations from the Ozone Monitoring Instrument (OMI) satellite sensor to infer top-down NO<sub>x</sub> emissions in the regional Weather Research and Forecasting model with coupled chemistry (WRF-Chem) and to evaluate the impact on simulated surface O<sub>3</sub> with in situ observations. We first perform a simulation for July 2015 over Europe and evaluate its performance against in situ observations from the AirBase network. The spatial distribution of mean ozone concentrations is reproduced satisfactorily. However, the simulated maximum daily 8 h ozone concentration (MDA8 O<sub>3</sub>) is underestimated (mean bias error of  $-14.2 \mu\text{g m}^{-3}$ ), and its spread is too low. We subsequently derive satellite-constrained surface NO<sub>x</sub> emissions using a mass balance approach based on the relative difference between OMI and WRF-Chem NO<sub>2</sub> columns. The method accounts for feedbacks through OH, NO<sub>2</sub>'s dominant daytime oxidant. Our optimized European NO<sub>x</sub> emissions amount to 0.50 Tg N (for July 2015), which is 0.18 Tg N higher than the bottom-up emissions (which lacked agricultural soil NO<sub>x</sub> emissions). Much of the increases occur across Europe, in regions where agricultural soil NO<sub>x</sub> emissions dominate. Our best estimate of soil NO<sub>x</sub> emissions in July 2015 is 0.1 Tg N, much higher than the bottom-up 0.02 Tg N natural soil NO<sub>x</sub> emissions from the Model of Emissions of Gases and Aerosols from Nature (MEGAN). A simulation

with satellite-updated NO<sub>x</sub> emissions reduces the systematic bias between WRF-Chem and OMI NO<sub>2</sub> (slope = 0.98,  $r^2 = 0.84$ ) and reduces the low bias against independent surface NO<sub>2</sub> measurements by  $1.1 \mu\text{g m}^{-3}$  ( $-56\%$ ). Following these NO<sub>x</sub> emission changes, daytime ozone is strongly affected, since NO<sub>x</sub> emission changes particularly affect daytime ozone formation. Monthly averaged simulated daytime ozone increases by  $6.0 \mu\text{g m}^{-3}$ , and increases of  $> 10 \mu\text{g m}^{-3}$  are seen in regions with large emission increases. With respect to the initial simulation, MDA8 O<sub>3</sub> has an improved spatial distribution, expressed by an increase in  $r^2$  from 0.40 to 0.53, and a decrease of the mean bias by  $7.4 \mu\text{g m}^{-3}$  ( $48\%$ ). Overall, our results highlight the dependence of surface ozone on its precursor NO<sub>x</sub> and demonstrate that simulations of surface ozone benefit from constraining surface NO<sub>x</sub> emissions by satellite NO<sub>2</sub> column observations.

## 1 Introduction

Ozone (O<sub>3</sub>) is an air pollutant that affects human and ecosystem health (Lelieveld et al., 2015; Ainsworth et al., 2012). It also affects radiative forcing directly as a greenhouse gas (IPCC, 2013) and indirectly by impacting ecosystem carbon uptake via deposition (Sitch et al., 2007). Despite decreases in ozone concentrations in Europe starting from 2000 (Chang et al., 2017), peak ozone concentrations still exceed the World Health Organization (WHO) air quality guideline of  $100 \mu\text{g m}^{-3}$  and the European long-term objective of  $120 \mu\text{g m}^{-3}$  (EMEP/CCC, 2016). For example, 87 % of European air quality stations did not meet this long-term objec-

tive (EEA, 2017) in 2015, and vegetation exposure thresholds were exceeded in large parts of the continent during this year, particularly in southern and central Europe (Rouïl and Meleux, 2018).

The formation of ozone in the lower troposphere is a photochemical process that depends non-linearly on concentrations of its precursor species nitrogen oxides (NO<sub>x</sub> = NO + NO<sub>2</sub>) and volatile organic compounds (VOCs) (e.g., Sillman et al., 1990). In NO<sub>x</sub>-limited conditions, ozone production increases with NO<sub>x</sub> emissions and is less sensitive to VOC emissions. However, ozone production under NO<sub>x</sub>-saturated conditions increases with VOC emissions but decreases with increasing NO<sub>x</sub> emissions. European NO<sub>x</sub> emissions are dominated by the anthropogenic contribution from fossil fuel combustion for transportation, electricity generation and industry. In summer, there are additional contributions from soils and lightning, which together comprise 40 % of the total European NO<sub>x</sub> emission budget (Jaeglé et al., 2005). Soil NO<sub>x</sub> emissions in turn have an anthropogenic component, since nitrogen-containing fertilizers are partly re-emitted to the atmosphere as NO<sub>x</sub> (Steinkamp and Lawrence, 2011).

Anthropogenic emissions in Europe have decreased due to air pollution abatement measures and the economic crisis that started in 2008 (Castellanos and Boersma, 2012). Bottom-up anthropogenic emission inventories suggest a continued reduction of NO<sub>x</sub> emissions in more recent years. This is consistent with the ongoing development of European air quality conditions towards the NO<sub>x</sub>-limited regime (Jin et al., 2017), which is projected to continue in the future (Beekmann and Vautard, 2010). Downward anthropogenic emission trends have also been suggested as an important driver of the decreasing trend in peak ozone concentrations in Europe (ETC/ACM, 2016).

Regional air quality (AQ) models are important tools for studying and forecasting ozone pollution. These models simulate processes relevant for ozone pollution at a resolution that can better capture observed spatial gradients compared to coarser global models. Regional AQ models can therefore be applied to simulate polluted conditions in or surrounding urban areas or for air quality impact assessments. Coupled (or “online”) meteorology–chemistry models resolve meteorology, transport, chemical transformation and removal of pollutants at the same spatial and temporal resolution. The coupled treatment of meteorology and chemistry is mandatory, because ozone concentrations depend on feedbacks between meteorological and chemical processes: (1) O<sub>3</sub> sources such as chemical formation depend on radiation, temperature and water vapor (Pusede et al., 2015; Coates et al., 2016), and (2) O<sub>3</sub> sinks, such as dry deposition, also largely depend on meteorological drivers (Clifton et al., 2017; Kavassalis and Murphy, 2017). However, coupled regional air quality models are subject to several sources of uncertainties. These uncertainties are related to the limited knowledge on ozone precursor emissions (Kuenen et al., 2014; Pouliot et al., 2015), the representation of boundary

conditions (Giordano et al., 2015), tropospheric chemistry in the chemical mechanism (Knote et al., 2015) and the land surface and its feedbacks with tropospheric chemistry (Baklanov et al., 2014).

Many regional AQ models have been applied to simulate NO<sub>x</sub> and O<sub>3</sub> in European summers, for research and forecasting purposes. Models tend to underestimate summertime NO<sub>x</sub> compared to rural background in situ observations (Terrenoire et al., 2015; Mar et al., 2016). Comparison against satellite NO<sub>2</sub> column observations also revealed underestimations at regional scales (Huijnen et al., 2010; Aidaoui et al., 2015). Another study found both positive as well as negative biases, which were attributed to the coarse resolution of the emission inventories (Pope et al., 2015). AQ models satisfactorily reproduce the spatial distribution in summer O<sub>3</sub>. However, mean O<sub>3</sub> can be under- or overestimated depending on the model and chemical mechanism (Terrenoire et al., 2015; Mar et al., 2016). In addition, many models consistently underestimate peak ozone values that typically occur in the afternoon (Tuccella et al., 2012; Solazzo et al., 2012; Marécal et al., 2015; Im et al., 2015). This is problematic for air pollution impact assessments, since the peak ozone values are important for determining the detrimental effects on human health and ecosystems.

The sensitivity of O<sub>3</sub> to its precursor NO<sub>x</sub>, which is particularly pronounced in summer (e.g., Jin et al., 2017), suggests that there is good potential to improve O<sub>3</sub> simulations by constraining simulated NO<sub>x</sub> with observations. The past 20 years have seen the development of methods to estimate NO<sub>x</sub> emissions with satellite-based NO<sub>2</sub> columns in a mass balance approach, where biases in the model-simulated and satellite-observed NO<sub>2</sub> columns are used to update NO<sub>x</sub> emissions. The technique has been applied in global models (Martin et al., 2003; Lamsal et al., 2008; Vinken et al., 2014a) and more recently also in regional models (e.g., Ghude et al., 2013). Applications of the technique include emission trend analysis (e.g., Lamsal et al., 2011) and source-specific constraints on NO<sub>x</sub> emissions (e.g., Ghude et al., 2013; Vinken et al., 2014a, b; Verstraeten et al., 2015). Changes in NO<sub>x</sub> emissions impact tropospheric chemistry, and therefore changes in O<sub>3</sub> are expected. This was shown by Ghude et al. (2013), who found local changes in surface O<sub>3</sub> mole fractions up to 10 ppb over India after satellite-based NO<sub>x</sub> emission scaling. Verstraeten et al. (2015) reported ozone increases up to 8 ppb at 800 hPa (±1.5 km) in China after scaling local NO<sub>x</sub> emissions with Ozone Monitoring Instrument (OMI) observations and found that simulated free-tropospheric ozone between 3 and 9 km was in better agreement with tropospheric O<sub>3</sub> columns observed by the Tropospheric Emission Sounder (TES). However, ozone changes at the surface after constraining NO<sub>x</sub> emissions with satellite observations have thus far not been evaluated with in situ data to our knowledge.

Considering the importance of NO<sub>x</sub> for simulations of ozone and the previously reported ozone changes after ap-

plying satellite-based NO<sub>x</sub> emissions, we here investigate the potential improvement in simulated surface ozone concentrations over Europe due to the application of satellite observations of NO<sub>2</sub> to adjust NO<sub>x</sub> emissions. To this end, we use the Weather Research and Forecasting model with coupled chemistry (WRF-Chem) (Grell et al., 2005) to simulate surface ozone in Europe in July 2015, at the approximate peak of the ozone season. We first perform a model evaluation with AirBase in situ NO<sub>2</sub> and O<sub>3</sub> observations (EEA, 2018) and OMI NO<sub>2</sub> column measurements from the recently released Quality Assurance for Essential Climate Variables (QA4ECV) dataset (Boersma et al., 2017a). We subsequently derive a new, OMI-based (“top-down”) NO<sub>x</sub> emission inventory and evaluate its effects on WRF-Chem simulations of surface NO<sub>2</sub> and O<sub>3</sub> with the independent AirBase observations.

The structure of the paper is as follows. We describe the model setup and observations in Sect. 2. Section 3 presents the method to calculate OMI-derived NO<sub>x</sub> emissions. In Sect. 4, we evaluate a WRF-Chem setup with bottom-up emissions in situ and column observations, and in Sect. 5 we describe the derived modified surface NO<sub>x</sub> emissions. We evaluate the impacts on surface NO<sub>x</sub> and O<sub>3</sub> with independent in situ observations in Sect. 6. We conclude with a discussion (Sect. 7) and summarize our conclusions in Sect. 8.

## 2 Model and data description

### 2.1 WRF-Chem

We perform simulations with the coupled meteorology–chemistry model WRF-Chem, version 3.7.1 (Grell et al., 2005). The model domain consists of 170 by 170 cells at 20 × 20 km<sup>2</sup> horizontal resolution covering Europe, centered at 51.98° N and 5.66° E. Vertically, the domain extends from the Earth’s surface up to 50 hPa and consists of 27 layers with 13 layers in the lowermost 1500 m. Chemistry simulations of O<sub>3</sub> and its precursor groups (NO<sub>x</sub> and VOCs) are performed with the Carbon Bond Mechanism Z (CBM-Z) gas-phase chemical mechanism (Zaveri and Peters, 1999). Simulations of atmospheric chemistry with this mechanism compare well with the European multi-model mean for summer O<sub>3</sub> in a gas-phase mechanism comparison study (Knote et al., 2015). A complete list of parameterization options adopted in our WRF-Chem setup can be found in Table S1 of the Supplement. Our simulations were performed with a time stepping of 180 s for a period of 38 d (24 June–31 July 2015), allowing a 1-week spin-up to analyze the model output for July. An evaluation of large-scale meteorological performance with ERA-Interim reanalysis fields can be found in Sect. S2 of the Supplement.

We used anthropogenic emissions from the Netherlands Organisation for Applied Scientific Research – Monitoring Atmospheric Composition and Climate (TNO-MACC-III)

inventory (Kuenen et al., 2014) for 2011, the most recent inventory available when the model experiments were performed. TNO-MACC-III contains anthropogenic emissions for lumped species groups (NO<sub>x</sub> and VOCs). NO<sub>x</sub> emissions were partitioned assuming that 97 % is emitted as NO and 3 % as NO<sub>2</sub>. VOC emissions were divided over 15 emission categories in CBM-Z, following the VOC speciation by Archer-Nicholls et al. (2014). This speciation procedure is further described in Table S3 of the Supplement. Point-source emissions were distributed over the five lowermost model layers following sector-specific emission altitude profiles (Bieser et al., 2011).

Biogenic emissions of VOCs and soil NO<sub>x</sub> were calculated online with the Model of Emissions of Gases and Aerosols from Nature (MEGAN) implementation within WRF-Chem (Guenther et al., 2006, 2012). The domain-total biogenic isoprene emissions are 1.82 Tg of isoprene, which is slightly lower than the 9-year spread of 2–4.5 Tg isoprene for July, based on an inverse modeling study using OMI HCHO column measurements for 2005–2013 (Bauwens et al., 2016). We simulate lightning NO<sub>x</sub> emissions using a parameterization based on cloud-top height (Price and Rind, 1993; Wong et al., 2013), using a flash rate of 80 mol flash<sup>-1</sup> based on a recent satellite-based estimate (Pickering et al., 2016). Simulations with higher flash rates of 500 mol flash<sup>-1</sup> (Ott et al., 2010) and 310 mol flash<sup>-1</sup> (Miyazaki et al., 2014) resulted in overestimated upper-tropospheric contributions to the NO<sub>2</sub> columns relative to OMI.

Anthropogenic emissions are the dominant NO<sub>x</sub> source over Europe in July, with a total monthly emission strength of 304 Gg N (76 %). Minor contributions are associated with lightning (81.4 Gg N; 20 %) and soils (15.0 Gg N; 4 %). We note that especially soil NO<sub>x</sub> emissions are low compared to previous studies, in which soils, including agricultural areas, have been estimated to contribute 40 % to the total European NO<sub>x</sub> emission budget (Jaeglé et al., 2005; Ganzeveld et al., 2010).

Meteorological initial and boundary conditions were taken from ERA-Interim reanalysis data (Dee et al., 2011). Chemical boundary conditions for O<sub>3</sub>, NO, NO<sub>2</sub>, CO and peroxyacetyl nitrate (PAN) are taken from the Copernicus Atmosphere Monitoring Service (CAMS) chemical reanalysis product for Europe (Inness et al., 2015, retrieved at <http://apps.ecmwf.int/datasets/data/cams-nrealtime/levtype=sfc/> (last access: 18 September 2019)). Upper boundary conditions for ozone were prescribed with climatological values (retrieved at <https://www2.acom.ucar.edu/wrf-chem/wrf-chem-tools-community>, last access: 17 September 2019).

### 2.2 AirBase NO<sub>2</sub> and O<sub>3</sub> in situ measurements

Surface measurements are taken from the European Air Quality Data Portal operated by the European Environment Agency, hereafter referred to as AirBase (EEA, 2018). We

used all data at rural background stations from the validated E1a data stream. The large availability of the data allows us to make a strict selection on data availability. For monthly averages, we discard stations if data are missing for more than 24 h. Stations used for the evaluation of monthly averages at 12:00 UTC may have a maximum data gap of one data point. This resulted in a final selection of 184–397 stations, depending on the performance metric (see Table 1). In our analysis of O<sub>3</sub> and NO<sub>2</sub>, we evaluate monthly time series and midday (12:00 UTC) concentrations (denoted as [O<sub>3</sub>]<sup>12h</sup> and [NO<sub>2</sub>]<sup>12h</sup>, respectively). We additionally calculate the maximum daily 8 h mean ozone concentration (MDA8 O<sub>3</sub>), a widely applied metric for O<sub>3</sub> health impacts.

### 2.3 OMI NO<sub>2</sub> column measurements

We use tropospheric NO<sub>2</sub> columns from OMI aboard NASA's Earth Observing System (EOS) Aura mission (Levell et al., 2006). The polar-orbiting instrument detects radiation backscattered from the Earth's atmosphere. Retrieval of tropospheric vertical column densities (VCDs) from space follows a three-step procedure (Boersma et al., 2018). First, total slant columns (SCDs; i.e., columns along the average light path through the atmosphere) are obtained from a spectral fit to the OMI-measured reflectance spectra in the visible wavelength range using the differential optical absorption spectroscopy (DOAS) method. Then, the stratospheric contribution component is separated from the total NO<sub>2</sub> column via data assimilation into the TM5 global chemistry transport model (Dirksen et al., 2011). The final step is to obtain tropospheric VCDs by dividing the SCDs by a tropospheric air mass factor (AMF) that describes the vertical sensitivity of the instrument to atmospheric NO<sub>2</sub> (Eskes and Boersma, 2003). This is a function of satellite viewing geometry, surface albedo, terrain height, cloud properties and a priori NO<sub>2</sub> profile.

The recent EU FP7 QA4ECV project has led to the development of a new OMI NO<sub>2</sub> data product (Boersma et al., 2017a). The underlying consortium retrieval algorithm is based on the NO<sub>2</sub> column retrieval principles described in Boersma et al. (2007) but with improvements in the three aforementioned steps (Boersma et al., 2018). Zara et al. (2018) described how better wavelength calibration and inclusion of liquid water absorption and an intensity offset correction reduced uncertainties in NO<sub>2</sub> SCDs to 0.7–0.8 × 10<sup>15</sup> molec. cm<sup>-2</sup> (up to ±35 %). Lorente et al. (2017) improved the AMF calculation method via the extension of the AMF look-up table with more reference points and a correction for the sphericity of the atmosphere. The ancillary data for the AMF calculation have also improved relative to earlier algorithms such as DOMINO v2 (Boersma et al., 2011): surface albedo from the 5-year OMI albedo climatology (Kleipool et al., 2008), cloud information from the improved OMI O<sub>2</sub>–O<sub>2</sub> algorithm (Veefkind et al., 2016) and a priori NO<sub>2</sub> profiles from TM5-MP at 1° × 1° (Williams

et al., 2017). The study by Lorente et al. (2017) also showed that substantial differences between AMFs arise when different a priori NO<sub>2</sub> profiles (as well as surface albedo and cloud properties) are used in the retrieval. This underlines that a recalculation of the tropospheric AMFs based on simulated WRF-Chem NO<sub>2</sub> profiles at 20 × 20 km<sup>2</sup>, replacing the coarse TM5-MP 1° × 1° NO<sub>2</sub> profiles, may help to reduce model–satellite differences (Lamsal et al., 2010; Vinken et al., 2014b), and we will explore this further below.

### 2.4 AMF recalculation

We take care to remove inconsistencies in the model–satellite comparison introduced by different assumptions about the vertical NO<sub>2</sub> profile in the satellite product compared to the model. The AMF calculation requires assumptions about the vertical profile of NO<sub>2</sub> to convert slant columns into vertical columns. We replace the a priori TM5-MP NO<sub>2</sub> profiles (at 1° × 1°) by WRF-Chem NO<sub>2</sub> profiles at a 20 × 20 km<sup>2</sup> resolution. This has two advantages: (1) model–satellite comparisons are no longer affected by differences in model assumptions between WRF-Chem and TM5-MP that lead to different vertical NO<sub>2</sub> profiles, and (2) the higher-resolution WRF-Chem setup resolves spatial gradients in the a priori profile that are not appropriately captured in TM5-MP due to the coarser model resolution. Single-orbit results indicate that recalculation of the AMFs leads to retrieved columns that are 1 × 10<sup>15</sup> molec. cm<sup>-2</sup> higher in densely populated areas and lower or unaffected in surrounding non-urban regions. This effect has been seen before in earlier studies (Huijnen et al., 2010; Heckel et al., 2011; Russell et al., 2011; Maasakkers, 2013; Vinken et al., 2014b).

We apply the method described by Lamsal et al. (2010) and Boersma et al. (2016) to replace the TM5-MP vertical NO<sub>2</sub> profile by the WRF-Chem profile in the calculation of the AMF:

$$M_{\text{trop,WC}} = M_{\text{trop,TM5}} \times \frac{\sum_{l=1}^L A_{\text{trop},l} x_{l,\text{WC}}}{\sum_{l=1}^L x_{l,\text{WC}}}, \quad (1)$$

where  $M_{\text{trop}}$  is the tropospheric AMF based on an assumed profile from WRF-Chem (WC) or TM5,  $A_{\text{trop},l}$  is the tropospheric averaging kernel element for layer  $l$ ,  $x_{l,\text{WRF-Chem}}$  is the NO<sub>2</sub> column density in model layer  $l$ , and  $L$  is the uppermost TM5-MP layer in the troposphere. The tropospheric averaging kernel in Eq. (1) is defined as follows (Boersma et al., 2017b):  $A_{\text{trop}} = A \times \frac{M}{M_{\text{trop}}}$ , where  $M$  and  $M_{\text{trop}}$  refer to the AMF and the tropospheric AMF, respectively. Note that the WRF-Chem vertical NO<sub>2</sub> profile has been sampled at the TM5-MP vertical layer structure, so  $l$  refers to TM5-MP model layers.

**Table 1.** Performance statistics of WRF-Chem bottom-up and top-down simulations for July 2015 for several conventionally applied performance metrics (mean bias error (MBE), RMSE, slope and intercept of a linear regression fit of simulations against observations, and  $r^2$  from orthogonal distance regression), as well as the index of agreement ( $d = 1 - \frac{\sum_{i=1}^N (P_i - O_i)^2}{\sum_{i=1}^N (|P_i| + |O_i|)^2}$ ; Willmott, 1982), where  $P_i$  and  $O_i$  represent simulations and observations, respectively. MBE, RMSE and intercept are in units of  $\mu\text{g m}^{-3}$ ; slope,  $r^2$  and  $d$  are unitless.

	$n$	Bottom-up						Top-down					
		MBE	RMSE	Slope	Intercept	$r^2$	$d$	MBE	RMSE	Slope	Intercept	$r^2$	$d$
$\overline{[\text{O}_3]}$	289	-2.37	2.50	0.26	54.27	0.32	0.60	2.18	17.03	0.34	53.23	0.41	0.68
$\overline{[\text{O}_3]}^{12\text{h}}$	397	-15.07	24.68	0.33	51.63	0.43	0.63	-7.56	19.09	0.41	51.13	0.58	0.74
MDA8 O <sub>3</sub>	289	-14.24	24.79	0.28	55.98	0.40	0.61	-7.38	19.99	0.36	55.72	0.53	0.70
$\overline{[\text{NO}_2]}$	184	-2.49	3.86	0.73	-0.28	0.42	0.70	-1.09	3.09	0.89	-0.12	0.46	0.80
$\overline{[\text{NO}_2]}^{12\text{h}}$	250	-2.96	3.56	0.30	-0.03	0.25	0.51	-2.59	3.28	0.33	0.04	0.23	0.53

### 3 Top-down NO<sub>x</sub> emissions: methods

Satellite-detected NO<sub>2</sub> columns are sensitive to NO<sub>x</sub> emissions at the surface. We exploit this dependence to derive satellite-based surface NO<sub>x</sub> emissions using local OMI NO<sub>2</sub> columns. We apply an improved version of the mass balance procedure (Martin et al., 2003; Lamsal et al., 2011; Vinken et al., 2014b), which accounts for non-linear feedback from NO<sub>x</sub> emission changes on NO<sub>2</sub> concentrations via OH:

$$E_{\text{td}} = E_{\text{bu}} \left( 1 + \beta(1 + \gamma) \frac{C_{\text{OMI, bu}} - C_{\text{WC, bu}}}{C_{\text{WC, bu}}} \right), \quad (2)$$

where  $E_{\text{bu}}$  and  $E_{\text{td}}$  represent NO<sub>x</sub> emissions from the bottom-up inventory (bu) and the satellite-based top-down estimate (td), respectively.  $C_{\text{WC, bu}}$  represents the monthly averaged NO<sub>2</sub> vertical column density (VCD) simulated by WRF-Chem, and  $C_{\text{OMI, bu}}$  is the monthly averaged modified QA4ECV OMI NO<sub>2</sub> VCD using air mass factors based on the original WRF-Chem NO<sub>2</sub> vertical profile ( $C_{\text{WC, bu}}$ ; see Sect. 2.4). WRF-Chem NO<sub>2</sub> VCDs are co-sampled with valid OMI observations. We only use OMI and WRF-Chem data for pixels with valid satellite observations for at least 4 d in July 2015 to minimize the random error in the satellite retrieval.

We account for the non-linear NO<sub>x</sub>-OH chemistry feedback via a dimensionless scaling factor  $\beta$ , for which we performed a perturbation simulation with surface emissions increased by 20%:

$$\beta = \frac{\Delta E_{\text{bu, 1.2}}/E_{\text{bu}}}{\Delta C_{\text{bu, 1.2}}/C_{\text{bu}}} = \frac{0.2C_{\text{bu}}}{\Delta C_{\text{bu, 1.2}}}, \quad (3)$$

where  $C_{\text{bu}}$  are the NO<sub>2</sub> columns after a WRF-Chem simulation with bottom-up NO<sub>x</sub> emissions, and  $\Delta C_{\text{bu, 1.2}}$  is the change in NO<sub>2</sub> columns after perturbing bottom-up NO<sub>x</sub> emissions by +20%. In low-NO<sub>x</sub> environments, this perturbation leads to higher OH levels and thus to more efficient NO<sub>x</sub> loss to HNO<sub>3</sub>, so that a  $\beta > 1$  is needed to achieve column agreement. In NO<sub>x</sub>-rich environments, however, OH

levels are suppressed by enhanced NO<sub>x</sub> emissions so that the relative increase in NO<sub>2</sub> columns is larger than 20%, resulting in a  $\beta < 1$ . The use of  $\beta$  to account for the sensitivity of the NO<sub>2</sub> column to local emissions is essentially a linearization step of non-linear effects due to chemistry.

Application of Eqs. (2) and (3) would lead to updated NO<sub>x</sub> emissions and consequently also to modifications in the WRF-Chem NO<sub>2</sub> profile shapes in response to the updates (e.g., Vinken et al., 2014b). This is accounted for via  $\gamma$ , which we also obtain from the simulation with +20% perturbed emissions:

$$\gamma = \frac{(C_{\text{OMI, 1.2}} - C_{\text{OMI, bu}})/C_{\text{OMI, bu}}}{(C_{\text{WC, 1.2}} - C_{\text{WC, bu}})/C_{\text{WC, bu}}}, \quad (4)$$

where  $C_{\text{WC}}$  represents the WRF-Chem NO<sub>2</sub> vertical column density (VCD), and  $C_{\text{OMI}}$  represents the OMI NO<sub>2</sub> VCD retrieved using WRF-Chem NO<sub>2</sub> vertical profiles from the bottom-up simulation ( $C_{\text{WC}}$ ), for the bottom-up (subscript bu) and emission perturbation simulation (subscript 1.2), respectively. Our approach to calculate  $\gamma$  differs from Vinken et al. (2014b), who derived  $\gamma$  from a separate simulation after accounting for  $\beta$ . Our approach requires one less forward simulation and is thus computationally more efficient, with little impact (< 3%) on total derived emissions compared to the approach by Vinken et al. (2014b).

We calculate the scaling factors  $\beta$  and  $\gamma$  for all land-based and shipping lane WRF-Chem cells based on monthly mean NO<sub>2</sub> columns (i.e., ocean-based pixels with emissions above a threshold value of  $1 \text{ mol km}^{-2} \text{ h}^{-1}$ ). These pixels thus also include shipping lanes and offshore oil platforms. OMI-inferred emission changes are calculated locally, i.e., for each individual model cell for which the aforementioned data availability criteria are fulfilled. This differs from previous work where these factors were calculated for regions containing multiple model cells (Vinken et al., 2014a, b) or for individual pixels in global models with a coarse resolution (e.g., Lamsal et al., 2011).

We discard the effect of transport of NO<sub>2</sub> away from the source region (“smearing”). In July, solar intensity in Europe

is close to its annual peak, which means that the NO<sub>2</sub> lifetime is short due to efficient oxidation. Therefore, the clear-sky monthly mean NO<sub>2</sub> column difference between model and satellite is indicative of local NO<sub>x</sub> emission updates. Previous studies showed that this method reduces the model–satellite NO<sub>2</sub> column difference but does not resolve it completely (e.g., Vinken et al., 2014b; Ghude et al., 2013) as a result of the linearization that is applied in the perturbation calculation. Nonetheless, we will show in this study that the systematic bias between WRF-Chem and OMI NO<sub>2</sub> columns is largely removed after application of Eqs. (2)–(4).

## 4 Bottom-up model evaluation

### 4.1 Surface O<sub>3</sub>

We start our evaluation of O<sub>3</sub> chemistry in WRF-Chem (with bottom-up NO<sub>x</sub> emissions, i.e., not yet based on the OMI-inferred NO<sub>x</sub> emissions) by a comparison of monthly averaged 24 h mean surface ozone simulations with AirBase observations (Fig. 1a and b; Table 1). WRF-Chem reproduces the spatial distribution of surface ozone satisfactorily, with an increase in surface O<sub>3</sub> concentrations from north to south, as reported elsewhere (e.g., Mar et al., 2016). Highest concentrations are found around the Mediterranean basin. O<sub>3</sub> concentrations over central and southern Europe are underestimated in WRF-Chem. Simulated monthly averaged concentrations do not exceed 110 µg m<sup>-3</sup>, while higher concentrations were observed at several stations in the southern part of the domain. Most notably, WRF-Chem does not capture observed high concentrations of ±130 µg m<sup>-3</sup> in northern Italy. The good agreement between WRF-Chem and in situ data in the western part of the domain close to the model boundaries with a prevailing westerly circulation indicates that the model boundary conditions describe inflow of long-lived compounds such as O<sub>3</sub> from the western boundary well.

Monthly averaged ozone concentrations are an important and widely used metric to evaluate model skill but are not necessarily indicative of the peak ozone concentrations that typically occur in the afternoon. These monthly averages include the nocturnal conditions with generally the presence of stable boundary layers, in which the titration of ozone in the NO<sub>x</sub>-saturated regions is difficult to model (e.g., Im et al., 2015). The simulated and observed monthly averaged ozone concentrations at 12:00 UTC (Fig. 1c, d) demonstrate a similar geographical distribution compared to the monthly average but with higher values because photochemical ozone production generally peaks during daytime. This figure demonstrates that peak ozone values occur around the Mediterranean basin, most prominently in northern Italy and Spain, where the levels of sunlight and ozone precursor concentrations are high. WRF-Chem shows elevated ozone with respect to adjacent areas, but maximum simulated ozone levels do not exceed 120 µg m<sup>-3</sup>. This underestimation of peak

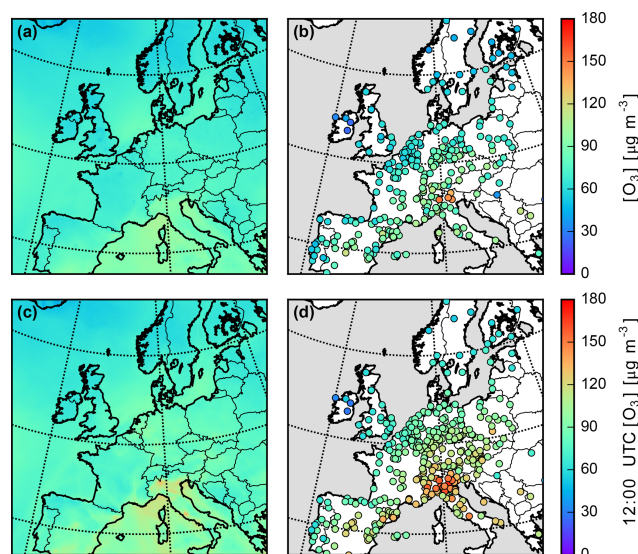


**Figure 1.** Monthly averaged surface O<sub>3</sub> and simulated by WRF-Chem with bottom-up NO<sub>x</sub> emissions (a, c) and observed at AirBase stations (b, d). Panels (a) and (b) are monthly averages, and (c) and (d) are sampled at 12:00 UTC.

ozone concentrations is also apparent from in Fig. 8b (discussed in more detail in Sect. 6), which shows the simulated versus the observed 12:00 UTC ozone concentrations.

Our results are in agreement with previous regional chemistry model evaluations for Europe. Such studies typically focus on seasonal variability; we compare our results with the results for European summer (JJA) from those studies. Im et al. (2015) found that a model ensemble underestimates the daytime maximum O<sub>3</sub> concentration for sites where observed O<sub>3</sub> concentrations exceed 120–140 µg m<sup>-3</sup>, which agrees with our results. In that study, the ensemble mean model bias tends to become more negative for observed concentrations above 80 µg m<sup>-3</sup> (Im et al., 2015). The two ensemble members that use CBM-Z chemistry, similar to our WRF-Chem model setup, are qualitatively in line with the ensemble mean, lending support to the use of CBM-Z in this study. Mar et al. (2016) compared two chemical mechanisms in a WRF-Chem evaluation study over Europe and reported large differences in the representation of peak summer (JJA) ozone: one chemistry model (MOZART) overestimates mean and MDA8 ozone, while simulations with the other chemistry scheme (RADM2) shows underestimations of peak ozone that are in line with our findings. We will discuss the dependence of ozone simulation on the chemical mechanism choice in detail in Sect. 7. The ensemble model mean daytime ozone concentration in Solazzo et al. (2012) is underestimated by 10–30 µg m<sup>-3</sup> in four subregions of the European continent. Tuccella et al. (2012) analyzed WRF-Chem O<sub>3</sub> concentrations for 2007 and found that yearly averaged midday ozone is underestimated by approximately 10 µg m<sup>-3</sup>. The model performance in the aforemen-

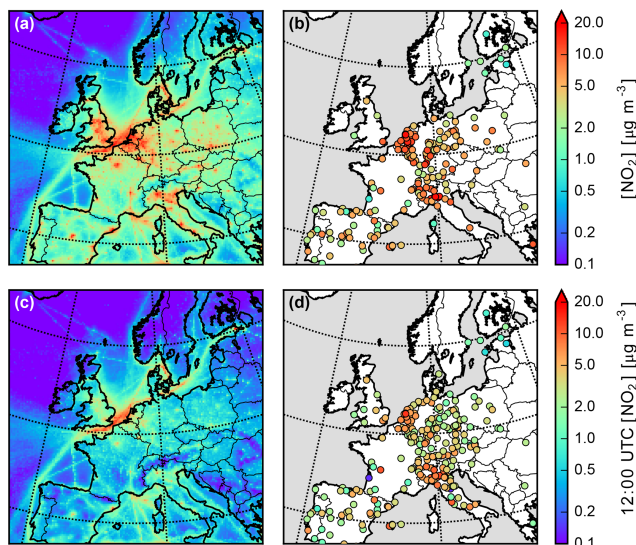


**Figure 2.** As Fig. 1 but for NO<sub>2</sub>.

tioned studies is qualitatively similar to our findings and the magnitude compares well. Overall, most studies consistently show underestimated daytime O<sub>3</sub>, regardless of the chemical mechanism, model resolution and other model assumptions. To further explore the potential role of a model misrepresentation of NO<sub>2</sub> concentrations in explaining this model O<sub>3</sub> bias, the next sections will focus on a model comparison with in situ and remote sensing data for NO<sub>2</sub>.

## 4.2 Surface NO<sub>2</sub>

Figure 2a and b present a comparison of monthly averaged surface concentrations of NO<sub>2</sub> between WRF-Chem and AirBase (note the logarithmic scale). Performance statistics are shown in Table 1. We find that WRF-Chem reproduces the spatial distribution well, with peak NO<sub>2</sub> occurring in northwest Europe and northern Italy. In these regions with high NO<sub>x</sub> emissions, average WRF-Chem-simulated concentrations are however underestimated by up to 10 µg m<sup>-3</sup> compared to observations. AirBase concentrations show a region with elevated NO<sub>2</sub> concentrations in southwest Germany. WRF-Chem also shows elevated NO<sub>2</sub> concentrations in this region but does not reach such elevated concentrations. Overall, WRF-Chem shows more spatial heterogeneity in surface NO<sub>2</sub> concentrations than is apparent from the observations. Observed NO<sub>2</sub> concentrations in background areas in Spain, France and eastern Europe are 2–5 µg m<sup>-3</sup> or higher, while the model consistently simulates values < 2 µg m<sup>-3</sup> in these regions. This overall underestimation is also seen in Fig. 8, where the simulated daily mean NO<sub>2</sub> concentration is shown against AirBase observations. The model performance of our WRF-Chem setup is in line with previous WRF-Chem studies. Mar et al. (2016) found small overestimations (0.67–2.96 µg m<sup>-3</sup>) in mean NO<sub>2</sub>. Another study found an annual

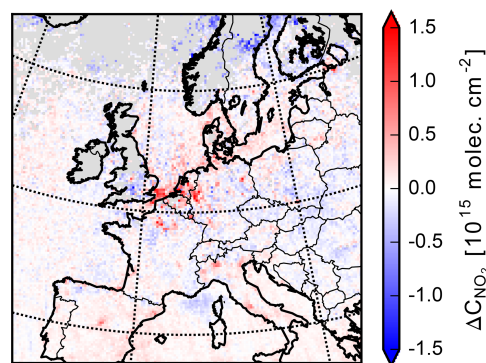


**Figure 3.** Change in monthly averaged OMI-retrieved NO<sub>2</sub> columns after using WRF-Chem vertical NO<sub>2</sub> profiles to calculate the air mass factors (AMFs) in the OMI retrieval, as described in Sect. 2.4.

average mean bias of  $-0.9 \mu\text{g m}^{-3}$ , caused by underestimations of peak NO<sub>2</sub> in WRF-Chem (Tuccella et al., 2012).

A comparison between WRF-Chem and AirBase monthly averaged 12:00 UTC NO<sub>2</sub> concentrations is presented in Fig. 2c and d and Table 1. We find that WRF-Chem on average strongly underestimates midday NO<sub>2</sub> concentrations by  $2.96 \mu\text{g m}^{-3}$  (38.5 %).

## 4.3 NO<sub>2</sub> VCD

Before we perform a comparison between NO<sub>2</sub> VCDs from WRF-Chem and OMI, we first discuss the effect of the NO<sub>2</sub> profile shape on the OMI-retrieved columns. Figure 3 shows the change in the monthly averaged OMI NO<sub>2</sub> column density after replacing TM5-MP NO<sub>2</sub> profiles by WRF-Chem profiles using the procedure described in Sect. 2.4. The OMI NO<sub>2</sub> VCDs change most prominently over urban/industrial areas such as the Netherlands, Paris, Berlin, Madrid, Milan and Rome. The background areas are largely unaffected or show small ( $\pm 0.2 \times 10^{15} \text{ molec. cm}^{-2}$ ) NO<sub>2</sub> VCD increases (e.g., Spain) or decreases (regions in France, Germany, Poland, Ukraine and Romania). The vertical NO<sub>2</sub> profile over sea regions in western Europe strongly peaks at the surface, because shipping NO<sub>x</sub> in WRF-Chem is emitted in the lowermost model layer. Overall, the average NO<sub>2</sub> column change over non-land regions is small (< 2 %).

We subsequently compare WRF-Chem to this modified OMI product. The monthly averaged NO<sub>2</sub> vertical column densities from WRF-Chem and OMI are displayed in Fig. 4. The model is sampled at 12:00 UTC, close to the OMI overpass time of  $\pm 13:30 \text{ LT}$ , and is co-sampled with valid satellite observations. There is good agreement in the spatial distribution of monthly averaged NO<sub>2</sub> VCDs ( $r^2 = 0.68$ ). NO<sub>2</sub> columns are underestimated by  $0.3 \times 10^{15} \text{ molec. cm}^{-2}$  on average, with strong underestimations of up to  $2 \times 10^{15} \text{ molec. cm}^{-2}$  in urban and industrial northwestern Europe. WRF-Chem overestimates NO<sub>2</sub> columns in some iso-

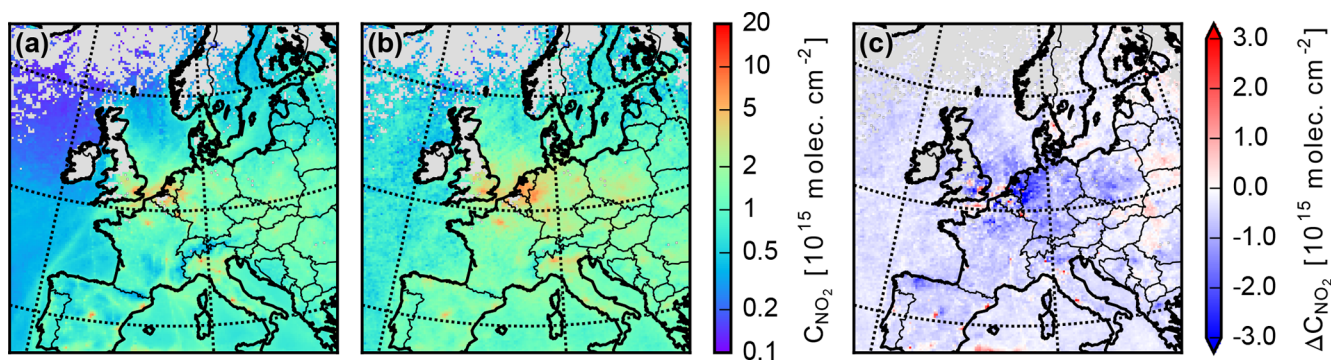


**Figure 4.** Monthly averaged tropospheric NO<sub>2</sub> vertical column densities from (a) WRF-Chem with bottom-up NO<sub>x</sub> emissions, (b) OMI and (c) their difference (WRF-Chem – OMI). WRF-Chem NO<sub>2</sub> columns have been co-sampled with OMI, and pixels are shown when  $n_{\text{obs}} \geq 4$ .

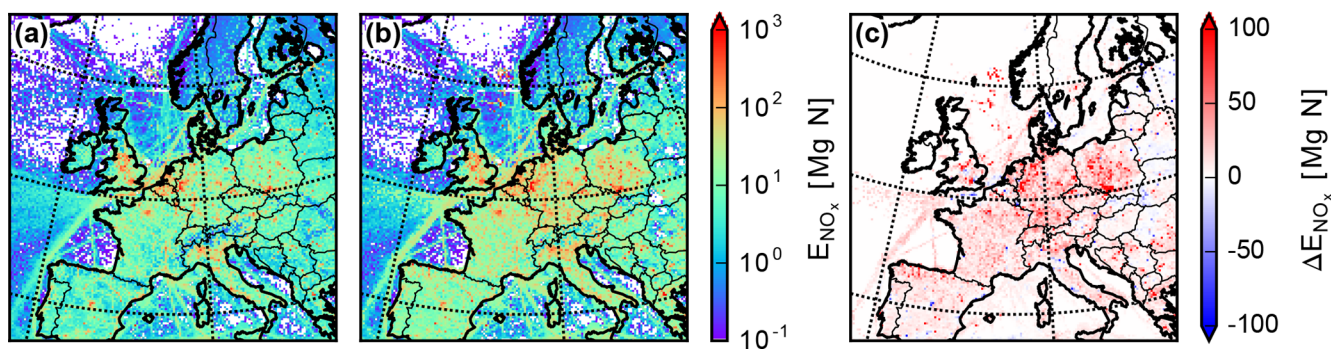


**Figure 5.** Surface NO<sub>x</sub> emissions for (a) the bottom-up simulation (TNO-MACC-III anthropogenic plus MEGAN soil NO<sub>x</sub> emissions) and (b) the top-down simulation; panel (c) depicts the change in surface NO<sub>x</sub> emissions after the recalculation procedure.

lated urban areas with high NO<sub>x</sub> emissions such as London, Madrid, Rome and in parts of eastern Europe.

We note that Fig. 4 shows small underestimations of the simulated NO<sub>2</sub> VCD compared to OMI ( $\pm 0.2 \times 10^{15}$  molec. cm<sup>-2</sup>) in background regions (e.g., the Alps, rural Spain and France, Scandinavia) and over the oceans. Simulated NO<sub>2</sub> columns therefore show stronger spatial gradients than OMI-retrieved columns, which is in line with Huijnen et al. (2010). Other distinct underestimations in the simulated NO<sub>2</sub> columns compared to OMI indicate a misrepresentation of emissions. For example, the simulated NO<sub>2</sub> column in northwestern Spain is underestimated by  $2 \times 10^{15}$  molec. cm<sup>-2</sup> compared to OMI. The enhanced NO<sub>2</sub> columns in this region mainly reflect the contribution to atmospheric NO<sub>x</sub> by power plant emissions. Although emissions from power plants should have decreased in recent years in this region (Zhou et al., 2012), these emissions seem to be underestimated in WRF-Chem. However, since these results are only representative of July 2015, a more dedicated analysis is needed to further corroborate this hypothesis.

We have shown that our WRF-Chem setup with bottom-up emissions underestimates NO<sub>2</sub> with respect to both surface and column measurements. To combine these model comparisons against different data sources, we already discuss

parts of Fig. 9, which compares the agreement between simulations with bottom-up and top-down emissions. Figure 9a shows the relative difference of WRF-Chem against AirBase and OMI NO<sub>2</sub> binned as a function of bottom-up anthropogenic emission strength. This shows an overall underestimation of WRF-Chem at the surface and in the troposphere, except for regions with strongest emissions. There is a relatively larger model underestimation of surface NO<sub>2</sub> than of the NO<sub>2</sub> VCD in regions with comparatively low emissions. Given that the surface NO<sub>2</sub> mixing ratios are more sensitive to surface emissions than the NO<sub>2</sub> column (Li and Wang, 2019), this suggests that emissions are generally too low in WRF-Chem, but especially that emissions in rural background regions are underestimated. This, in turn, suggests that the representation of surface NO<sub>x</sub> emissions in WRF-Chem (anthropogenic emissions for 2011 and online calculated natural soil emissions) are too low to explain the observations in July 2015. In the following section, we will derive satellite-constrained NO<sub>x</sub> emissions and discuss potential reasons for this mismatch.



## 5 Satellite-derived NO<sub>x</sub> emissions

### 5.1 Top-down emissions

We derive top-down NO<sub>x</sub> emissions using the method described in Sect. 3. Figure 5 shows the July total bottom-up and top-down surface NO<sub>x</sub> emissions and their difference. Top-down NO<sub>x</sub> emissions amount to 498 Gg N, which is 56 % higher than the bottom-up inventory, and increases occur across the domain (Fig. 5c). NO<sub>x</sub> emissions are reduced in several isolated grid cells that generally correspond to urban areas. The difference between top-down and bottom-up emissions is larger than the 16 % increase reported by Miyazaki et al. (2017), although that study found strong (40 %–67 %) local increases in areas with high NO<sub>x</sub> emissions such as Belgium, western Germany and northern Italy.

Our top-down emissions are much higher than the bottom-up emissions over Germany and Poland. Over Belgium and the Netherlands, the difference between top-down and bottom-up emissions is also substantial but notably smaller despite larger differences between OMI and WRF-Chem NO<sub>2</sub> columns over the low countries (Fig. 4c). This reflects the chemical regime with very high bottom-up NO<sub>x</sub> emissions in this region, resulting in suppressed midday OH concentrations and consequently longer NO<sub>2</sub> lifetimes (as diagnosed by low beta values over northwestern Europe in Fig. S1 of the Supplement).

We subsequently replace bottom-up emissions with our observation-constrained top-down NO<sub>x</sub> emissions and perform a new WRF-Chem simulation. As expected, the new NO<sub>2</sub> columns agree much better with the OMI NO<sub>2</sub> columns than those from the simulation with bottom-up emissions (Fig. 6). WRF-Chem with bottom-up emissions generally underestimates OMI NO<sub>2</sub> columns by 23.4 %. As expected, the simulations with the top-down emissions agree better with OMI, and the slope of 0.98 between the new WRF-Chem and OMI NO<sub>2</sub> columns (Fig. 6b) suggests that the systematic underestimation in the model is effectively resolved by applying the top-down emissions. The mean relative error is reduced to −7.5 %, and the spatial correlation coefficient between WRF-Chem and OMI NO<sub>2</sub> also improves considerably (from 0.68 to 0.84).

### 5.2 Attribution to emission sources

Figure 7 shows the bottom-up and top-down NO<sub>x</sub> emissions as a function of the bottom-up anthropogenic emission strength. This comparison demonstrates that top-down NO<sub>x</sub> emissions are higher than bottom-up emissions regardless of the emission strength. However, top-down emissions are 50 %–100 % higher than bottom-up estimates for relatively weak emissions between 0.5 and 50 Mg N month<sup>−1</sup> cell<sup>−1</sup> and only up to 20 % higher for some urban and industrial hotspots (Fig. 7b). This 0.5–50 Mg N month<sup>−1</sup> range is dominated by WRF-Chem grid cells located in the rural areas

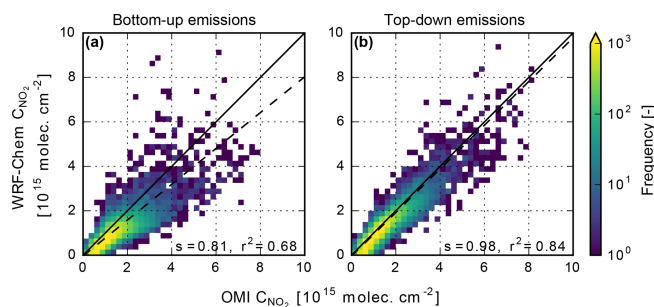


**Figure 6.** NO<sub>2</sub> vertical column density scatter plots of WRF-Chem against OMI, presented as a heat map with a bin size of  $0.25 \times 10^{15}$  molec. cm<sup>−2</sup> for WRF-Chem with bottom-up emissions (a) and WRF-Chem with OMI-derived top-down surface NO<sub>x</sub> emissions (b). The OMI NO<sub>2</sub> VCDs in panels (a) and (b) are calculated with AMFs based on NO<sub>2</sub> vertical profiles of the WRF-Chem simulations against which they are compared, to ensure a consistent model–satellite comparison. The solid black lines represent the 1 : 1 line, and the dashed lines display the orthogonal distance regression fits.

of Europe, excluding the largest urban agglomerations as well as low-emission regions such as mountainous areas. Our substantially larger top-down emissions partly reflect a required increase in NO<sub>x</sub> emissions in areas where soil NO emissions are expected to be a dominant NO<sub>x</sub> source. Soil NO emissions are simulated in WRF-Chem using an implementation of the MEGAN biogenic emission model. The observed discrepancy between the WRF-Chem-simulated and OMI-observed NO<sub>2</sub> VCD triggers to assess how much of this discrepancy can be attributed to this model's representation of soil NO emissions.

To separate the soil NO<sub>x</sub> contribution from the anthropogenic emission updates, we perform a simple budget calculation as a first-order constraint on the partitioning of the top-down emissions between their anthropogenic and soil-based sources. We assume that the relative difference in anthropogenic sources is uniform over the emission bins in Fig. 7. This factor is calculated as the median of the relative change in emissions for the three highest bins (> 50 Mg N cell<sup>−1</sup> for July; see Fig. 7) and amounts to 0.22. This allows us to attribute the remaining emission difference to soils. Based on this crude first estimate, we derive top-down soil NO<sub>x</sub> emissions to be 112 Gg N month<sup>−1</sup> versus WRF-Chem/MEGAN-simulated bottom-up soil NO emissions of only 15 Gg N month<sup>−1</sup>. The anthropogenic enhancement factor is relatively uncertain but does not strongly impact our derived posterior soil NO<sub>x</sub> emission estimate: if, instead of the median ( $m = 0.22$ ), we use the mean relative change in emissions for the three highest bins ( $\mu = 0.41$ ), our soil contribution is still a factor > 4 larger (69.0 Gg N month<sup>−1</sup>) compared to WRF-Chem's simulated bottom-up soil NO source. Therefore, this first-order estimation suggests that a substan-

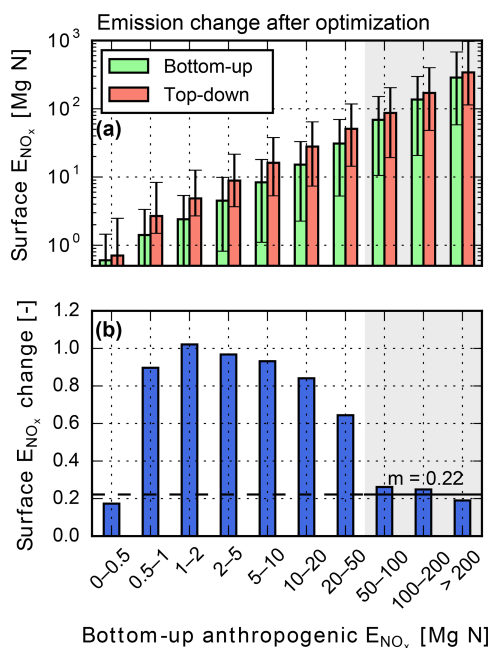


**Figure 7.** Difference between bottom-up and top-down surface NO<sub>x</sub> emissions, expressed as (a) a bar plot (note the logarithmic scale) of median emissions binned by bottom-up anthropogenic NO<sub>x</sub> emissions (error bars indicate the interquartile range) and (b) a bar plot of relative emission differences  $\left(\frac{\text{posterior} - \text{prior}}{\text{prior}}\right)$  between the bars in panel (a). In panel (b) we define the relative anthropogenic emission difference to be the median of the relative change between top-down and bottom-up emissions in anthropogenic-dominated regions (shaded, with bottom-up emissions > 50 Mg N month<sup>-1</sup> cell<sup>-1</sup>).

tial fraction (43 %–69 %) of the NO<sub>x</sub> emission increment after optimization can be attributed to soils.

To evaluate the derived total soil NO<sub>x</sub> emissions, we perform a comparison with literature-based estimates in Table 2. We find that bottom-up soil NO<sub>x</sub> emissions are underestimated by a factor of 5–7 compared to previous studies. In some of those studies (e.g., Ganzeveld et al., 2010), land use management practices (fertilizer and manure application) provide a substantial contribution to European soil NO emissions, a feature that appears to be missing in the representation of soil NO emissions in WRF-Chem. This supports our hypothesis that a substantial fraction of the increase in surface NO<sub>x</sub> emissions may be attributed to soils. We will discuss this further in Sect. 7.

## 6 Emission scaling impacts on surface NO<sub>2</sub> and O<sub>3</sub>

### 6.1 Nitrogen dioxide

Table 1 summarizes the model performance of our bottom-up and top-down WRF-Chem simulations against a large number of AirBase NO<sub>2</sub> observations throughout Europe

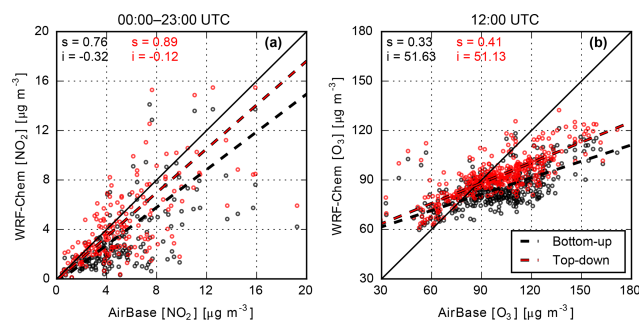


**Figure 8.** Scatter plots of monthly averaged simulated concentrations of (a) NO<sub>2</sub> and (b) O<sub>3</sub> against AirBase observations. Panel (a) shows monthly averages for 00:00–23:00 UTC, while panel (b) is sampled at 12:00 UTC. The black solid lines represent the 1 : 1 line.

in July 2015. The simulation with top-down emissions improves upon the a priori run in all metrics. Most notably, the model index of agreement (*d*) improves by 0.10 (14 %). The modified model setup still slightly underestimates the monthly averaged observed NO<sub>2</sub> observations, as indicated by a slope of 0.89. However, the low bias in WRF-Chem surface NO<sub>2</sub> concentrations with respect to AirBase improves from  $-2.5$  to  $-1.1 \mu\text{g m}^{-3}$ .

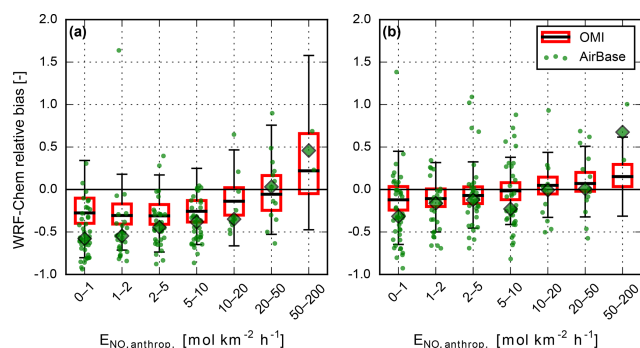
Compared to the monthly average, we find little improvement in WRF-Chem's skill to predict surface NO<sub>2</sub> at 12:00 UTC. The model's low bias in NO<sub>2</sub> reduces from  $-3.0$  to  $-2.6 \mu\text{g m}^{-3}$  and the index of agreement improves by only 0.02 (4 %). This more modest improvement in performance can be understood from midday surface NO<sub>2</sub> concentrations being more strongly driven by photochemical removal processes and boundary layer development than the 24 h mean NO<sub>2</sub> levels, which are more sensitive to NO<sub>x</sub> emissions due to strongly reduced mixing and photochemistry at night. Figure 8 displays WRF-Chem monthly 24 h mean NO<sub>2</sub> concentrations against AirBase observations for the bottom-up (black) and top-down (red) simulations. The model orthogonal distance regression (ODR) slope improves considerably, while the explained variance of the model improves slightly to 0.46.

Figure 9 shows the relative biases between WRF-Chem and observed NO<sub>2</sub> as a function of (binned) bottom-up anthropogenic NO emission strength. Both the WRF-Chem simulations with bottom-up emissions (Fig. 9a) as well as the simulation with top-down emissions (Fig. 9b) show a low bias against OMI and AirBase for regions with low emissions and a positive relative bias in regions with stronger emissions. The relative bias is however considerably reduced in the simulation with top-down NO<sub>x</sub> emissions, both at the surface and in the column. However, WRF-Chem still displays a stronger relative bias compared to AirBase than compared to OMI. This feature can likely be attributed to a difference in spatial scales between the  $20 \times 20 \text{ km}^2$  resolution model and the footprint area of local AirBase measurements, which

**Table 2.** Comparison of WRF-Chem surface NO<sub>x</sub> emissions in July (in Tg N month<sup>-1</sup>, unless indicated otherwise) with literature-reported values.

	Year	Region	Surface	Anthropogenic	Soils	Soils (%)
This study, bottom-up	2015	Maps in this study	0.32	0.30	0.015	4.7
This study, top-down, after bias attribution (see Sect. 5.2)	2015	Maps in this study	0.50	0.39–0.43	0.07–0.11	14–22
Stohl et al. (1996)	1994	34.9–72.1° N, –24.6–41.9° E	–	–	–	17.6*
Ganzeveld et al. (2010)	2000	34–64° N, –16–41° E	–	–	0.14	–
Jaeglé et al. (2005)	2000	35–60° N, –15–45° E	0.59	0.35	0.25	42.3
Miyazaki et al. (2017)	2005–2014	35–60° N, –10–30° E	0.33–0.38	–	–	–
Dammers (2013)	2005–2007	35–70° N, –15–35° E	–	–	0.09	–
Lathière et al. (2005) referenced in Dammers (2013)	1983–1995	–15–35° E, 35–70° N	–	–	0.13	–

\* This estimate is based on summer (JJA) estimates.



**Figure 9.** Relative bias ( $RB = \frac{\text{model} - \text{observations}}{\text{observations}}$ ) of WRF-Chem against land-based OMI NO<sub>2</sub> vertical column densities (box plots) and AirBase in situ NO<sub>2</sub> measurements (green scatter), binned by bottom-up anthropogenic NO emission strength, for the bottom-up (a) and top-down (b) WRF-Chem simulations. Green diamonds indicate the median WRF-Chem RB against AirBase observations for pixels within every emissions bin.

can be easily influenced by a nearby NO<sub>x</sub> source that is less well captured in the model, due to instantaneous mixing over a larger volume. Another potential explanation for lower relative bias of WRF-Chem compared to AirBase than compared to OMI is interference of in situ measurements with molybdenum converters (see Sect. 2.2). This is in line with our previous finding that the slope of the top-down NO<sub>2</sub> column regression fit approaches 1, while the slope of the fit for in situ NO<sub>2</sub> observations is still below 1. We also note that the spread in the relative bias compared to AirBase increased for the top-down simulation, with more positive relative bias values for all bins. Nonetheless, the results shown in Fig. 9 provide confidence regarding application of the model as a tool to reconcile local-scale bottom-up emissions and concentrations with larger-scale remote-sensing-based NO<sub>2</sub> measurements.

## 6.2 Ozone

Next, we address our main question whether the improved simulation of NO<sub>2</sub> leads to better model performance for surface ozone simulations. We find that WRF-Chem with top-down emissions improves upon the bottom-up simulation for both the 24 h mean, as well as the 12:00 UTC and MDA8 ozone metrics. The model index of agreement improves by 0.08–0.11 (13%–17%; Table 1). However, the top-down model still simulates too-low surface O<sub>3</sub>, especially over southern, eastern and central Europe, where observed surface O<sub>3</sub> exceeds 80 μg m<sup>-3</sup> at 12:00 UTC (see Fig. 11).

A comparison between monthly averaged midday O<sub>3</sub> concentrations from the bottom-up and top-down simulations (Fig. 11a and b, respectively) shows that ozone increases across the model domain. This particularly improves the WRF-Chem–AirBase agreement in large parts of western and central Europe. The simulated ozone values in northern Italy remain underestimated.

Surface ozone concentrations display a strong increase due to the use of top-down NO<sub>x</sub> emissions (Fig. 11). The areas where ozone concentrations increase by > 10 μg m<sup>-3</sup> largely coincide with regions where top-down NO<sub>x</sub> emissions are much higher than the bottom-up emissions (Fig. 5c), such as in northern Spain, southern Germany, southern Poland, Croatia, Serbia, western Greece and southern Romania. There are also strong simulated ozone increases in central France and over the Adriatic Sea. These regions are all characterized as (rural) background areas, where ozone formation is strongly sensitive to the increases introduced in the NO<sub>x</sub> emissions for the relatively low bottom-up anthropogenic and soil emissions. We find decreases in ozone around the main shipping lanes, where the higher NO<sub>x</sub> emissions further enhance ozone titration. The enhanced titration also reduced simulated surface ozone around urban regions such as Barcelona, Rome and Paris. The increases in surface NO<sub>x</sub> emissions in

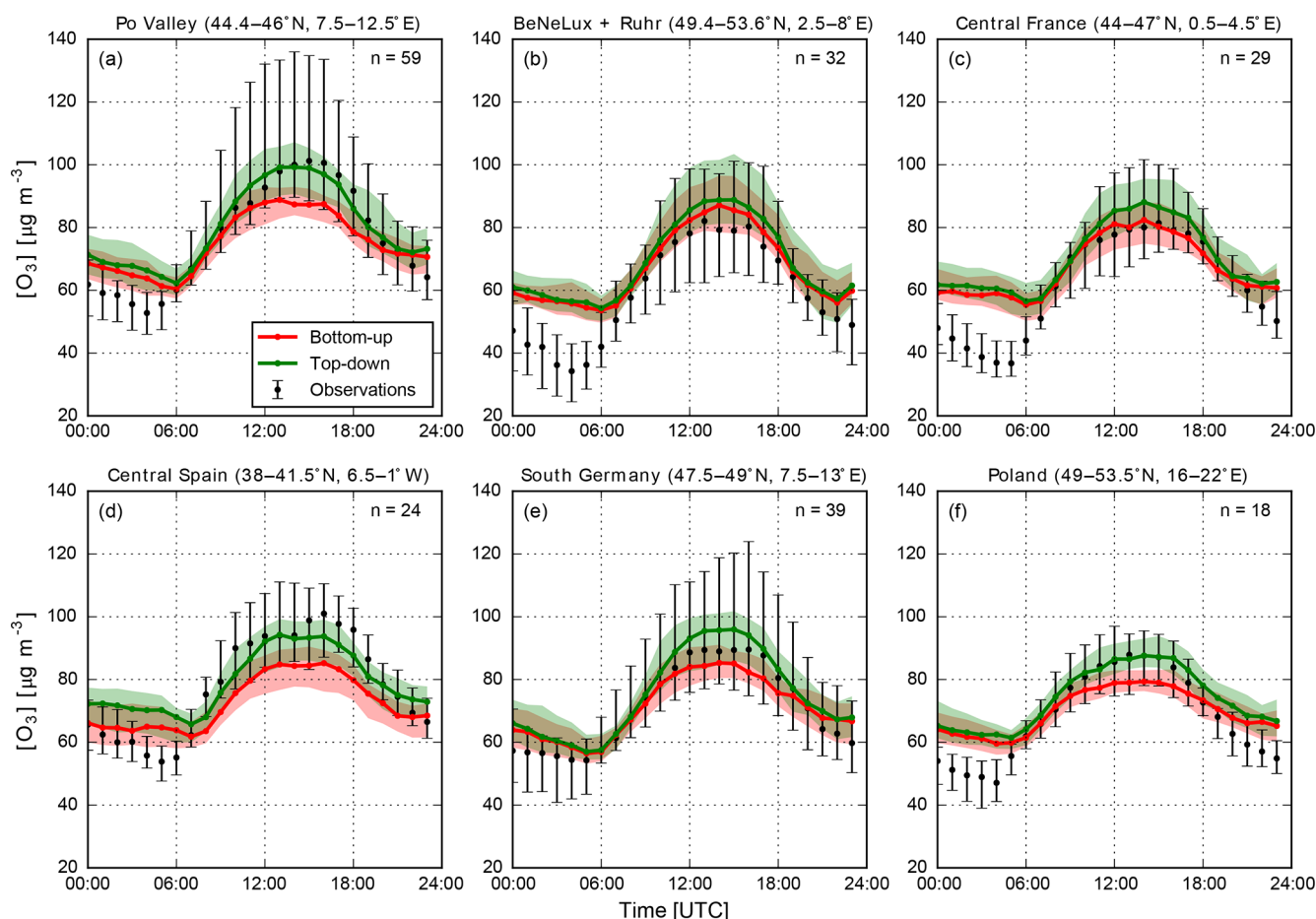


**Figure 10.** July 2015 monthly median diurnal ozone concentrations for six representative regions in Europe, as simulated by WRF-Chem with bottom-up NO<sub>x</sub> emissions (green line) and top-down NO<sub>x</sub> emissions (red line), and as observed at AirBase stations in these regions. Shaded areas and whiskers indicate the interquartile range. Results represent the median over all model–observation comparisons per region. The sample size for the comparison is displayed on the top right of each subplot.

the BeNeLux region and western Germany slightly increase simulated midday surface ozone. Ozone production is less sensitive to NO<sub>x</sub> emissions in these high NO<sub>x</sub>-emitting regions compared to the unpolluted background (Beekmann and Vautard, 2010; Mar et al., 2016; Jin et al., 2017).

Figure 8 shows that O<sub>3</sub> simulations with the higher top-down NO<sub>x</sub> emissions lead to a somewhat better match between modeled and observed surface O<sub>3</sub>, with an improvement in spatial correlation coefficient from 0.43 to 0.57, and an increase in slope from 0.33 to 0.41. Overall, the model low bias has reduced from  $-15$  to  $-8 \mu\text{g m}^{-3}$ , which indicates that the use of OMI NO<sub>2</sub> VCD data to constrain WRF-Chem surface NO<sub>x</sub> emissions results in a considerable improvement regarding simulation of surface layer O<sub>3</sub> concentrations.

We additionally analyzed changes in the temporal evolution of ozone concentrations resulting from NO<sub>x</sub> emission changes (Fig. 10). Daytime median O<sub>3</sub> concentrations are better captured in the Po Valley, central Spain and Poland.

The NO<sub>x</sub> emission changes lead to a model overestimation of surface O<sub>3</sub> concentrations for central France and south Germany, while concentrations change only slightly in the BeNeLux and Ruhr areas. In those regions, the mean bias error increases, while the hourly correlation coefficient and RMSE values improve for all regions (Table S4 of the Supplement). In all areas, changes in NO<sub>x</sub> emissions led to increased ozone concentrations particularly during daytime. Enhancements in simulated nighttime concentrations are only observed in central Spain. In other areas, nighttime O<sub>3</sub> concentrations are overestimated in both simulations. Peak daytime O<sub>3</sub> concentrations are better captured in all areas, as evidenced by the increase of the 75th percentile of simulated O<sub>3</sub> concentrations with top-down emissions. However, peak O<sub>3</sub> concentrations remain underestimated in the Po Valley, central Spain and southern Germany. Additionally, nighttime O<sub>3</sub> concentration overestimations remain, likely due to issues related to model resolution and vertical mixing. Overall, the NO<sub>x</sub> emission changes most ef-

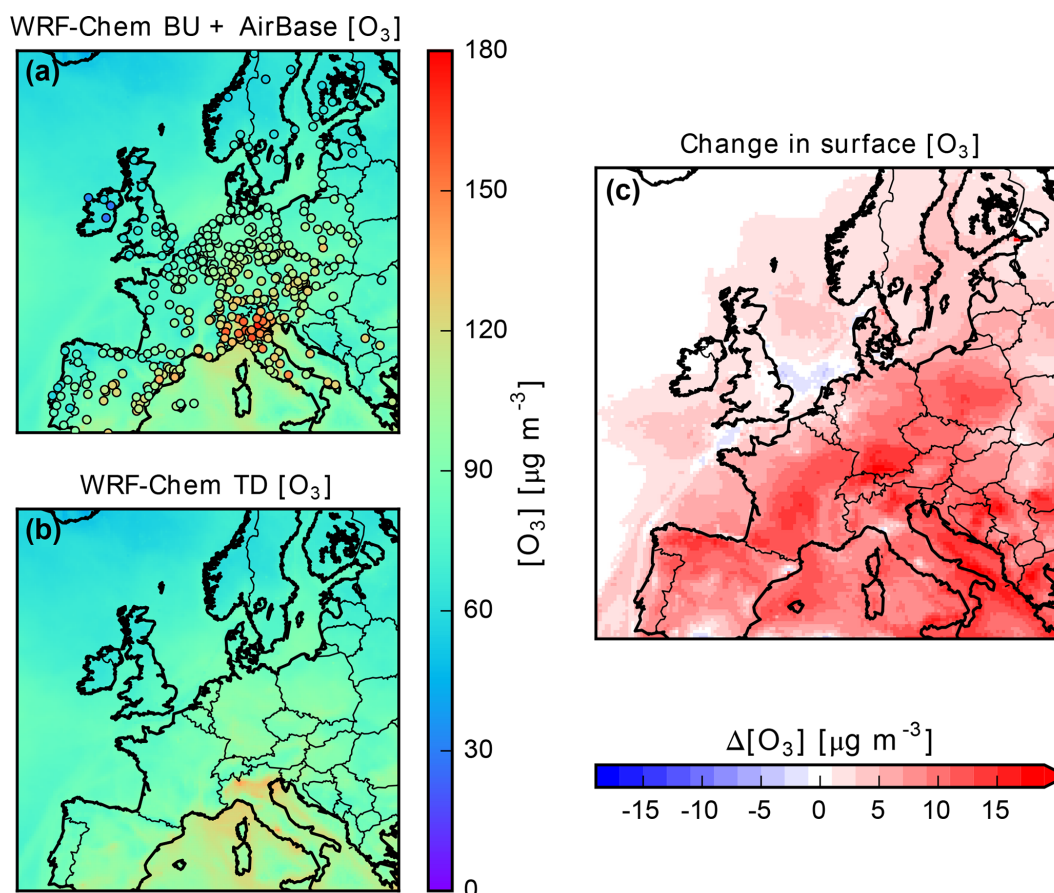


**Figure 11.** Monthly averaged 12:00 UTC surface  $\text{O}_3$  concentration with bottom-up (bu, panel a) and top-down (td, panel b)  $\text{NO}_x$  emissions. Panel (c) shows the difference between the two monthly averages (td–bu).

fectively increase  $\text{O}_3$  concentrations during periods with elevated ozone (Fig. S3 of the Supplement), which coincide with high solar radiation and temperatures and thus have a strongly  $\text{NO}_x$ -dependent  $\text{O}_3$  formation.

## 7 Discussion

In this study, we demonstrate the added value of deriving satellite-based  $\text{NO}_x$  emissions in (regional) air pollution models for simulations of summertime ozone, focusing on July 2015 over Europe. We use a modified version of the mass balance approach introduced by Martin et al. (2003), with further improvements by Lamsal et al. (2011) and Vinken et al. (2014b). Although many studies report differences in simulated (surface) ozone concentrations after applying this mass balance approach (e.g., Ghude et al., 2013), we are aware of only one other study that used observations to validate subsequent ozone changes. Verstraeten et al. (2015) used TES  $\text{O}_3$  observations in the global chemistry model TM5 in a study on transcontinental transport of Asian air pollution and found an improved model–satellite agreement in lower-tropospheric ozone. However, their ap-

proach did not allow for an evaluation of model performance closer to the surface.

The mass balance approach that we used to derive observation-constrained European  $\text{NO}_x$  emissions has several important advantages over more formal inversion methods that are applied in the literature (e.g., Miyazaki et al., 2014, 2017). The method is highly traceable due to the simple calculation of scaling parameters from model output for a baseline and perturbation simulation, and column  $\text{NO}_2$  measurements. However, the linearization (see Sect. 3) oversimplifies the non-linearity of the  $\text{NO}_x$ – $\text{O}_3$  chemistry, which means that the model–satellite discrepancy is not resolved completely after one iteration. Additionally, the approach is only applicable on a pixel basis when the  $\text{NO}_x$  lifetime is sufficiently short to discard the contribution of transport from adjacent model  $\text{NO}_2$  columns. The model–satellite difference for a simulation we performed for March 2015 (not shown) shows less spatial heterogeneity over regions with a diffuse spatial distribution of  $\text{NO}_x$  sources (e.g., Germany). These shortcomings can be resolved by averaging the signal over multiple grid cells or by applying more formal inversion methods.

Our results demonstrate that surface NO<sub>x</sub> emissions in our WRF-Chem configuration are increased substantially after applying an emission scaling approach. In a first-order budget calculation, we derive that 43 %–69 % of this total increase can be attributed to soil NO<sub>x</sub>. This is diagnosed from the notably higher relative increase in emissions in regions with moderate anthropogenic emissions compared to regions with low and high anthropogenic emissions. We therefore conclude that the contribution of soil NO<sub>x</sub> to total surface emissions is likely underestimated in our model setup. Additionally, our top-down soil NO<sub>x</sub> emission estimate, derived with a budget calculation, agrees well with previous estimates for European summer (Table 2). Our findings are in line with a previous study (Oikawa et al., 2015) that, using WRF-Chem with MEGAN soil NO<sub>x</sub> emissions, found a strong underestimation of NO<sub>x</sub> emissions in a high-temperature agricultural region.

Several studies previously investigated the relation between soil NO<sub>x</sub> emissions and O<sub>3</sub> formation. For example, one study estimated that European soil NO<sub>x</sub> emissions contribute 4 ppb to the daily maximum concentration (Stohl et al., 1996). A sensitivity study by Li et al. (2019) indicates that a strong upscaling of soil NO<sub>x</sub> emissions by a factor of 5 indeed leads to a better representation of the peak ozone concentration. It has further been shown that an improved process-based representation of soil NO<sub>x</sub> emissions leads to MDA8 O<sub>3</sub> changes by up to 6 ppb (Rasool et al., 2016) and a reduced mean bias for ozone concentrations, particularly in agricultural areas (Rasool et al., 2019). Together, these findings provide support for the hypothesis that underestimated soil NO<sub>x</sub> emissions, in particular those from agricultural areas, contribute to underestimated peak ozone concentrations.

The comparison against in situ NO<sub>2</sub> observations from the AirBase network may be hindered by interference of reactive N species for measurements with molybdenum converters. The type of converter is not reported in the database. Literature-reported estimates of measurement overestimations due to this interference are 22 % (Dunlea et al., 2007) and 5 %–18 % (Boersma et al., 2009) at urban sites and 20 %–42 % at a rural site (Steinbacher et al., 2007). A correction factor can be applied to obtain corrected NO<sub>2</sub> measurements from observations using a molybdenum converter, which is on average 0.4–0.6 in summer, but with a large spread (0.2–0.8) (Lamsal et al., 2008, 2010). The strongest corrections of molybdenum-based in situ NO<sub>2</sub> measurements are needed in remote environments, where NO<sub>x</sub> is a relatively smaller component of the total reactive nitrogen budget compared to areas closer to NO<sub>x</sub> sources (Lamsal et al., 2008). We hypothesize that this can partially explain the remaining model–observation mismatch for NO<sub>2</sub> after the use of top-down emissions.

Despite the demonstrated improvement in ozone simulations, our simulation with OMI-derived top-down NO<sub>x</sub> emissions still misrepresents the high tail of the ozone distribution. We believe that there is a potential explanatory role

for local to regional meteorological processes. The representation of several mesoscale phenomena requires a higher model resolution than 20 × 20 km<sup>2</sup>. For example, Millán et al. (1997) demonstrated that local recirculation of residual air masses from higher aloft, containing elevated O<sub>3</sub> transported aloft during previous days, can be entrained in the boundary layer and contribute substantially to air pollution episodes in southern Europe. This is supported by an analysis of measured ozone (precursors) in northeast Spain by Querol et al. (2017), where this mesoscale circulation pattern was found to contribute to concentrations that exceed the information threshold value set by the European Union (180 μg m<sup>-3</sup>), alongside contributions from locally emitted NO<sub>x</sub> and biogenic VOCs.

Simulations of surface ozone in AQ models are also impacted by the choice of chemical parameterization. Recently, several studies have investigated the influence of the chemical mechanism on simulated NO<sub>x</sub> and O<sub>3</sub> concentrations. Regarding ozone chemistry, chemical mechanisms differ predominantly in two aspects: (1) the grouping of VOC species in species categories (“lumping”) according to their chemical structure or number of C atoms and (2) the inorganic rate coefficients involved in the catalytic cycling of NO<sub>x</sub>, HO<sub>x</sub> and O<sub>x</sub>. Especially the latter aspect has a strong influence on simulated NO<sub>2</sub> concentrations and can therefore influence the derivation of top-down emission estimates using satellite observations (Stavrakou et al., 2013). Coates et al. (2016) investigated the maximum ozone formation potential in different chemical mechanisms and found that mechanisms with lumped VOC categories led to lower ozone mixing ratios compared to a mechanism with a near-explicit treatment of VOCs. Knote et al. (2015) found small differences in inorganic rate constants among mechanisms and thus concluded that VOC representation was the dominating source of uncertainty among mechanisms. However, Mar et al. (2016) performed a WRF-Chem sensitivity study where MOZART inorganic rate constants were applied within RADM2, leading to mean O<sub>3</sub> concentration differences of 8 μg m<sup>-3</sup> between those mechanisms.

In order to test the importance of inorganic NO<sub>x</sub>–HO<sub>x</sub>–O<sub>x</sub> reaction rates for ozone formation, we implemented inorganic rate constants from three different mechanisms (CBM-Z, RADM2 and MOZART) in a mixed layer model with simplified chemistry (Janssen et al., 2012). Further details are given in Sect. S5 of the Supplement. Our analysis shows that varying the temperature-dependent rate constant of HNO<sub>3</sub> formation ( $k^{\text{NO}_2+\text{OH}}$ ) can lead to a spread of 2 ppb for end-of-afternoon ozone values on a typical summer day in a polluted boundary layer. CBM-Z uses the lowest  $k^{\text{NO}_2+\text{OH}}$  among the considered mechanisms and thus leads to a higher NO<sub>2</sub> lifetime and more O<sub>3</sub> formation than in other mechanisms. Therefore, we conclude that modification of inorganic reaction rate constants has a modest effect on simulated O<sub>3</sub> but is not likely to lead to increases in simulated O<sub>3</sub> in our WRF-Chem configuration. Nevertheless, the model repre-

resentation of ozone chemistry should be carefully considered in NO<sub>x</sub> and O<sub>3</sub> air quality studies, besides the representation of NO<sub>x</sub> emissions.

Several studies have considered the resolution dependence of air quality simulations. This is especially relevant for NO<sub>2</sub>, since NO<sub>x</sub> emissions display strong variation on the 20 × 20 km<sup>2</sup> scale applied in this study. Increasing model resolution leads to better representation of these local gradients and therefore improves simulations of NO<sub>2</sub> concentrations (Schaap et al., 2015). Valin et al. (2011) found that an accurate representation of midday NO<sub>2</sub> columns from highly localized sources requires a high model resolution, but regions with more diffuse sources can be simulated at a coarser resolution of ±10 × 10 km<sup>2</sup>. Although ozone production regimes do not strongly depend on the model resolution in regional models, high-resolution models perform better at simulating local O<sub>3</sub> titration in freshly emitted NO plumes (Cohan et al., 2006).

Besides the representation of meteorological processes, there is an additional uncertainty related to surface–atmosphere exchange of pollutants. Dry deposition constitutes 17 % of the tropospheric sink of ozone and is the second most important removal process after chemical removal (Hu et al., 2017). Several studies have recently investigated the role of meteorological drivers that determine ozone removal at the surface. However, these meteorological controls are oversimplified in deposition parameterizations. The vapor pressure deficit strongly controls stomatal uptake of ozone, thereby affecting surface ozone levels in spring to summer in the United States (Kavassalis and Murphy, 2017). Analysis of 10-year O<sub>3</sub> flux observations in the northeastern United States revealed that the removal of ozone by the land surface exhibits a strong interannual variability, which is not captured in dry deposition parameterizations (Clifton et al., 2017). Lastly, the role of soil moisture has been proposed as a regulator of surface ozone uptake (Tawfik and Steiner, 2013) and is often neglected in parameterizations of dry deposition, even though a recent study found that it can significantly reduce simulated ozone uptake (Anav et al., 2017). Improving the biophysical representation of the dry deposition process in WRF-Chem will be one of our foci in the future.

Future studies that apply satellite-based constraints on surface NO<sub>x</sub> emissions can benefit from observations from the recently launched TROPOspheric Monitoring Instrument (TROPOMI) instrument (Veefkind et al., 2012), which delivers NO<sub>2</sub> column data at an unprecedented resolution of 7 × 3.5 km<sup>2</sup>. This has the potential to lead to important improvements in satellite-constrained NO<sub>x</sub> emissions. Recent work (Lorente et al., 2019) has applied TROPOMI observations in a column model study to derive emissions from Paris. The resolution of the instrument additionally enables the focus on more local areas with one dominating source such as soils in agricultural or bare-soil regions.

## 8 Conclusions

We performed a WRF-Chem simulation of NO<sub>x</sub> and ozone over Europe for July 2015 and assessed its performance with AirBase in situ observations and OMI NO<sub>2</sub> column measurements. We find that WRF-Chem underestimates high surface ozone concentrations in central and southern Europe, and overestimates lower ozone concentrations in northern Europe. The model also underestimates the spread. The monthly averaged mean bias error (MBE) is relatively small (−2.4 μg m<sup>−3</sup>, 10 %). WRF-Chem underestimates daytime increases in ozone concentrations, as evidenced by substantial negative MBE values for the midday (12:00 UTC) O<sub>3</sub> concentration and MDA8 O<sub>3</sub> (−15.1 and −14.2 μg m<sup>−3</sup>, respectively). We relate the low bias in surface ozone to biases in ozone precursor concentrations. Of particular relevance are nitrogen oxides, which drive ozone production in much of NO<sub>x</sub>-limited summertime Europe.

For NO<sub>2</sub>, we find that WRF-Chem underestimates surface and column NO<sub>2</sub> values for most of the domain, with the exception of some high-emission regions. With respect to AirBase, WRF-Chem monthly averaged surface NO<sub>2</sub> is biased low by −2.5 μg m<sup>−3</sup> (−73 %). The spatial distribution of WRF-Chem column NO<sub>2</sub> agrees well with OMI ( $r^2 = 0.68$ ) and a mean underestimation of  $0.3 \times 10^{15}$  molec. cm<sup>−2</sup> (−23 %). We attribute the low bias in WRF-Chem NO<sub>2</sub> concentrations to underestimations in surface NO<sub>x</sub> emissions in WRF-Chem. We subsequently derive optimized NO<sub>x</sub> emissions based on the WRF-Chem/OMI relative difference using a mass balance approach. Overall emissions increase from 0.32 to 0.50 Tg N, an increase of 0.18 Tg N (+56 %), for July 2015. The updates indicate that NO<sub>x</sub> emissions should be scaled up across the domain. The relative increase in emissions is largest for regions with moderate emission strength (up to 50 Mg N month<sup>−1</sup> cell<sup>−1</sup>) and coincides with regions where agricultural soil NO<sub>x</sub> emissions are substantial. Our optimized soil NO<sub>x</sub> emissions amount to 0.1 Tg N, in much better agreement with values from the literature.

A WRF-Chem simulation with optimized NO<sub>x</sub> emissions removes the model's systematic bias with respect to OMI NO<sub>2</sub> and leads to an improved spatial agreement (slope = 0.98,  $r^2 = 0.84$ ). An evaluation against AirBase NO<sub>2</sub> reveals that the top-down simulation improves particularly in the monthly average, where the systematic mismatch is reduced (slope = 0.89 instead of 0.73) and the mean bias is reduced by 50 %. For ozone, the model skill improves particularly for midday and MDA8 O<sub>3</sub>, when local ozone formation occurs and the sensitivity of ozone formation to NO<sub>x</sub> concentrations is highest. On average, surface O<sub>3</sub> concentrations increase by 6 μg m<sup>−3</sup> (6 %). Still, peak (midday) ozone values are underestimated after NO<sub>x</sub> emission optimization.

Overall, our findings demonstrate that air quality model simulations combined with in situ and remote sensing observations can be used to infer missing sources of NO<sub>x</sub> at the surface. By optimizing NO<sub>x</sub> emissions with satellite obser-

vations, substantial improvements in simulated ozone can be achieved. Our work shows that this helps to reduce the persistent biases in O<sub>3</sub> that most air quality models are suffering from. Projected decreasing trends in anthropogenic NO<sub>x</sub> emissions will mean that the contribution of soils to total European NO<sub>x</sub> emissions will likely increase in the future and thus deserves careful attention in (European) air quality assessments, along with detailed assessments of emissions of volatile organic compounds and wildfires, boundary layer mixing and chemistry.

*Code and data availability.* WRF-Chem output and recalculated OMI NO<sub>2</sub> columns are available upon request, as well as scripts to recalculate the tropospheric AMF and the resulting changes in satellite NO<sub>2</sub> columns.

*Supplement.* The supplement related to this article is available online at: <https://doi.org/10.5194/acp-19-11821-2019-supplement>.

*Author contributions.* AJV, KFB and LNG designed the experiment. AJV performed the model simulations and analysis, with support from all co-authors. AJV wrote the manuscript, with contributions from all co-authors.

*Competing interests.* The authors declare that they have no conflict of interest.

*Acknowledgements.* The authors acknowledge the free availability of the WRF-Chem model (<https://www2.acom.ucar.edu/wrf-chem>, last access: 5 February 2019), in situ data from AirBase (<http://discomap.eea.europa.eu/map/fme/AirQualityExport.htm>, last access: 14 March 2019) and satellite NO<sub>2</sub> column observations from the OMI instrument (<http://www.qa4ecv.eu>, last access: 12 March 2019). We additionally thank John Paton for his help with downloading AirBase in situ measurements. Lastly, we thank three anonymous referees for their useful and constructive comments, which helped to improve this work.

*Financial support.* This research has been supported by the Dutch Research Council (NWO) and the Netherlands Space Office (NSO) under the User Support Programme Space Research (grant no. ALW-GO 16/17)

*Review statement.* This paper was edited by Pedro Jimenez-Guerrero and reviewed by three anonymous referees.

## References

- Aidaoui, L., Maurizi, A., and Azzi, A.: Modelled NO<sub>2</sub> tropospheric columns at different resolutions versus OMI satellite data: analysis of a 1-year BOLCHEM simulation over Europe, *Air Qual. Atmos. Health*, 8, 163–174, <https://doi.org/10.1007/s11869-015-0315-x>, 2015.
- Ainsworth, E. E. A., Yendrek, C. R., Sitch, S., Collins, W. J., and Emberson, L. D.: The effects of tropospheric ozone on net primary productivity and implications for climate change., *Annu. Rev. Plant Biol.*, 63, 637–61, <https://doi.org/10.1146/annurev-arplant-042110-103829>, 2012.
- Anav, A., Proietti, C., Menut, L., Carnicelli, S., De Marco, A., and Paoletti, E.: Sensitivity of stomatal conductance to soil moisture: implications for tropospheric ozone, *Atmos. Chem. Phys.*, 18, 5747–5763, <https://doi.org/10.5194/acp-18-5747-2018>, 2018.
- Archer-Nicholls, S., Lowe, D., Utembe, S., Allan, J., Zaveri, R. A., Fast, J. D., Hodnebrog, Ø., Denier van der Gon, H., and McFiggans, G.: Gaseous chemistry and aerosol mechanism developments for version 3.5.1 of the online regional model, WRF-Chem, *Geosci. Model Dev.*, 7, 2557–2579, <https://doi.org/10.5194/gmd-7-2557-2014>, 2014.
- Baklanov, A., Schlünzen, K., Suppan, P., Baldasano, J., Brunner, D., Aksoyoglu, S., Carmichael, G., Douros, J., Flemming, J., Forkel, R., Galmarini, S., Gauss, M., Grell, G., Hirtl, M., Joffe, S., Jorba, O., Kaas, E., Kaasik, M., Kallos, G., Kong, X., Korsholm, U., Kurganskiy, A., Kushta, J., Lohmann, U., Mahura, A., Manders-Groot, A., Maurizi, A., Moussiopoulos, N., Rao, S. T., Savage, N., Seigneur, C., Sokhi, R. S., Solazzo, E., Solomos, S., Sørensen, B., Tsegas, G., Vignati, E., Vogel, B., and Zhang, Y.: Online coupled regional meteorology chemistry models in Europe: current status and prospects, *Atmos. Chem. Phys.*, 14, 317–398, <https://doi.org/10.5194/acp-14-317-2014>, 2014.
- Bauwens, M., Stavrou, T., Müller, J.-F., De Smedt, I., Van Roozendaal, M., van der Werf, G. R., Wiedinmyer, C., Kaiser, J. W., Sindelarova, K., and Guenther, A.: Nine years of global hydrocarbon emissions based on source inversion of OMI formaldehyde observations, *Atmos. Chem. Phys.*, 16, 10133–10158, <https://doi.org/10.5194/acp-16-10133-2016>, 2016.
- Beekmann, M. and Vautard, R.: A modelling study of photochemical regimes over Europe: robustness and variability, *Atmos. Chem. Phys.*, 10, 10067–10084, <https://doi.org/10.5194/acp-10-10067-2010>, 2010.
- Bieser, J., Aulinger, A., Matthias, V., Quante, M., and Denier Van Der Gon, H. A. C.: Vertical emission profiles for Europe based on plume rise calculations, *Environ. Pollut.*, 159, 2935–2946, <https://doi.org/10.1016/j.envpol.2011.04.030>, 2011.
- Boersma, K. F., Eskes, H. J., Veefkind, J. P., Brinkma, E. J., van der A, R. J., Sneep, M., van den Oord, G. H. J., Levelt, P. F., Stammes, P., Gleason, J. F., and Bucsela, E. J.: Near-real time retrieval of tropospheric NO<sub>2</sub> from OMI, *Atmos. Chem. Phys.*, 7, 2103–2118, <https://doi.org/10.5194/acp-7-2103-2007>, 2007.
- Boersma, K. F., Jacob, D. J., Trainic, M., Rudich, Y., DeSmedt, I., Dirksen, R., and Eskes, H. J.: Validation of urban NO<sub>2</sub> concentrations and their diurnal and seasonal variations observed from the SCIAMACHY and OMI sensors using in situ surface measurements in Israeli cities, *Atmos. Chem. Phys.*, 9, 3867–3879, <https://doi.org/10.5194/acp-9-3867-2009>, 2009.
- Boersma, K. F., Eskes, H. J., Dirksen, R. J., van der A, R. J., Veefkind, J. P., Stammes, P., Huijnen, V., Kleipool, Q. L., Sneep,



- M., Claas, J., Leitão, J., Richter, A., Zhou, Y., and Brunner, D.: An improved tropospheric NO<sub>2</sub> column retrieval algorithm for the Ozone Monitoring Instrument, *Atmos. Meas. Tech.*, 4, 1905–1928, <https://doi.org/10.5194/amt-4-1905-2011>, 2011.
- Boersma, K. F., Vinken, G. C. M., and Eskes, H. J.: Representativeness errors in comparing chemistry transport and chemistry climate models with satellite UV–Vis tropospheric column retrievals, *Geosci. Model Dev.*, 9, 875–898, <https://doi.org/10.5194/gmd-9-875-2016>, 2016.
- Boersma, K., Eskes, H. J., Richter, A., De Smedt, I., Lorente, A., Beirle, S., Van Geffen, J., Peters, E., Van Roozendaal, M., and Wagner, T.: QA4ECV NO<sub>2</sub> tropospheric and stratospheric vertical column data from OMI (Version 1.1) [Data set], <https://doi.org/10.21944/qa4ecv-no2-omi-v1.1>, 2017a.
- Boersma, K. F., Van Geffen, J., Eskes, H. J., van der A, R. J., De Smedt, I., van Roozendaal, M., Yu, H., Richter, A., Peters, E., Beirle, S., Wagner, T., Lorente, A., Scanlon, T., Compernelle, S., and Lambert, J.: Product specification document for the QA4ECV NO<sub>2</sub> ECV precursor product, Tech. Rep. D4.6, KNMI, De Bilt, the Netherlands, available at: <http://www.qa4ecv.eu/sites/default/files/D4.6.pdf> (last access: 25 June 2019), 2017b.
- Boersma, K. F., Eskes, H. J., Richter, A., De Smedt, I., Lorente, A., Beirle, S., van Geffen, J. H. G. M., Zara, M., Peters, E., Van Roozendaal, M., Wagner, T., Maasackers, J. D., van der A, R. J., Nightingale, J., De Rudder, A., Irie, H., Pinardi, G., Lambert, J.-C., and Compernelle, S. C.: Improving algorithms and uncertainty estimates for satellite NO<sub>2</sub> retrievals: results from the quality assurance for the essential climate variables (QA4ECV) project, *Atmos. Meas. Tech.*, 11, 6651–6678, <https://doi.org/10.5194/amt-11-6651-2018>, 2018.
- Castellanos, P. and Boersma, K. F.: Reductions in nitrogen oxides over Europe driven by environmental policy and economic recession., *Sci. Rep.*, 2, 265, <https://doi.org/10.1038/srep00265>, 2012.
- Chang, K.-L., Petropavlovskikh, I., Copper, O. R., Schultz, M. G., and Wang, T.: Regional trend analysis of surface ozone observations from monitoring networks in eastern North America, Europe and East Asia, *Elementa*, 5, 22, <https://doi.org/10.1525/elementa.243>, 2017.
- Clifton, O. E., Fiore, A. M., Munger, J. W., Malyshev, S., Horowitz, L. W., Shevliakova, E., Paulot, F., Murray, L. T., and Griffin, K. L.: Interannual variability in ozone removal by a temperate deciduous forest, *Geophys. Res. Lett.*, 44, 542–552, <https://doi.org/10.1002/2016GL070923>, 2017.
- Coates, J., Mar, K. A., Ojha, N., and Butler, T. M.: The influence of temperature on ozone production under varying NO<sub>x</sub> conditions – a modelling study, *Atmos. Chem. Phys.*, 16, 11601–11615, <https://doi.org/10.5194/acp-16-11601-2016>, 2016.
- Cohan, D. S., Hu, Y., and Russell, A. G.: Dependence of ozone sensitivity analysis on grid resolution, *Atmos. Environ.*, 40, 126–135, <https://doi.org/10.1016/j.atmosenv.2005.09.031>, 2006.
- Dammers, E.: Assessment of soil nitrogen oxides emissions and implementation in LOTOS-EUROS (MSc thesis), Eindhoven (NL), available at: <https://pure.tue.nl/ws/files/46932268/758935-1.pdf> (last access: 18 January 2019), 2013.
- Dee, D. P., Uppala, S. M., Simmons, A. J., Berrisford, P., Poli, P., Kobayashi, S., Andrae, U., Balmaseda, M. A., Balsamo, G., Bauer, P., Bechtold, P., Beljaars, A. C. M., van de Berg, L., Bidlot, J., Bormann, N., Delsol, C., Dragani, R., Fuentes, M., Geer, A. J., Haimberger, L., Healy, S. B., Hersbach, H., Hólm, E. V., Isaksen, I., Kållberg, P., Köhler, M., Matricardi, M., McNally, A. P., Monge-Sanz, B. M., Morcrette, J. J., Park, B. K., Peubey, C., de Rosnay, P., Tavolato, C., Thépaut, J. N., and Vitart, F.: The ERA-Interim reanalysis: Configuration and performance of the data assimilation system, *Q. J. Roy. Meteorol. Soc.*, 137, 553–597, <https://doi.org/10.1002/qj.828>, 2011.
- Dirksen, R. J., Boersma, K. F., Eskes, H. J., Ionov, D. V., Bucsela, E. J., Levelt, P. F., and Kelder, H. M.: Evaluation of stratospheric NO<sub>2</sub> retrieved from the Ozone Monitoring Instrument: Intercomparison, diurnal cycle, and trending, *J. Geophys. Res.-Atmos.*, 116, 1–22, <https://doi.org/10.1029/2010JD014943>, 2011.
- Dunlea, E. J., Herndon, S. C., Nelson, D. D., Volkamer, R. M., San Martini, F., Sheehy, P. M., Zahniser, M. S., Shorter, J. H., Wormhoudt, J. C., Lamb, B. K., Allwine, E. J., Gaffney, J. S., Marley, N. A., Grutter, M., Marquez, C., Blanco, S., Cardenas, B., Retama, A., Ramos Villegas, C. R., Kolb, C. E., Molina, L. T., and Molina, M. J.: Evaluation of nitrogen dioxide chemiluminescence monitors in a polluted urban environment, *Atmos. Chem. Phys.*, 7, 2691–2704, <https://doi.org/10.5194/acp-7-2691-2007>, 2007.
- EEA: Air quality in Europe – 2017 report, Tech. Rep. 13, European Environment Agency, Copenhagen, Denmark, <https://doi.org/10.2800/22775>, 2017.
- EEA: Air Quality e-Reporting [Data Set], available at: <https://www.eea.europa.eu/data-and-maps/data/aqereporting-8> (last access: 6 June 2019), 2018.
- EMEP/CCC: Air pollution trends in the EMEP region between 1990 and 2012, Tech. Rep. 1/2016, EMEP, Kjeller, NO, available at: <http://publications.iass-potsdam.de/pubman/item/escidoc:1622889:8/component/escidoc:1622890/1622889.pdf> (last access: 11 March 2019), 2016.
- Eskes, H. J. and Boersma, K. F.: Averaging kernels for DOAS total-column satellite retrievals, *Atmos. Chem. Phys.*, 3, 1285–1291, <https://doi.org/10.5194/acp-3-1285-2003>, 2003.
- ETC/ACM: Long term air quality trends in Europe: contribution of meteorological variability, natural factors and emissions, Tech. Rep. 2016/7, European Topic Centre on Air Pollution and Climate Change Mitigation, Bilthoven, NL, available at: [https://acm.eionet.europa.eu/reports/docs/ETCACM\\_TP\\_2016\\_7\\_AQTrendsEurope.pdf](https://acm.eionet.europa.eu/reports/docs/ETCACM_TP_2016_7_AQTrendsEurope.pdf) (last access: 11 March 2019), 2016.
- Ganzeveld, L., Bouwman, L., Stehfest, E., van Vuuren, D., Eickhout, B., and Lelieveld, J.: Impacts of future land cover changes on atmospheric chemistry-climate interactions, *J. Geophys. Res.*, 115, D23301, <https://doi.org/10.1029/2010JD014041>, 2010.
- Ghude, S. D., Pfister, G. G., Jena, C. K., van der A, R. J., Emmmons, L. K., and Kumar, R.: Satellite constraints of Nitrogen Oxide (NO<sub>x</sub>) emissions from India based on OMI observations and WRF-Chem simulations, *Geophys. Res. Lett.*, 40, 1–6, <https://doi.org/10.1029/2012GL053926>, 2013.
- Giordano, L., Brunner, D., Flemming, J., Hogrefe, C., Im, U., Bianconi, R., Badia, A., Balzarini, A., Baró, R., Chemel, C., Curci, G., Forkel, R., Jiménez-Guerrero, P., Hirtl, M., Hodzic, A., Honzak, L., Jorba, O., Knote, C., Kuenen, J. J., Makar, P. A., Manders-Groot, A., Neal, L., Pérez, J. L., Pirovano, G., Pouliot, G., San José, R., Savage, N., Schröder, W., Sokhi, R. S., Syrakov, D., Torian, A., Tuccella, P., Werhahn, J., Wolke, R., Yahya, K., Žabkar, R., Zhang, Y., and Galmarini, S.: Assessment of the MACC reanalysis and its influ-

- ence as chemical boundary conditions for regional air quality modeling in AQMEII-2, *Atmos. Environ.*, 115, 371–388, <https://doi.org/10.1016/j.atmosenv.2015.02.034>, 2015.
- Grell, G. A., Peckham, S. E., Schmitz, R., Mckeen, S. A., Frost, G., Skamarock, W. C., and Eder, B.: Fully coupled “online” chemistry within the WRF model, *Atmos. Environ.*, 39, 6957–6975, <https://doi.org/10.1016/j.atmosenv.2005.04.027>, 2005.
- Guenther, A., Karl, T., Harley, P., Wiedinmyer, C., Palmer, P. I., and Geron, C.: Estimates of global terrestrial isoprene emissions using MEGAN (Model of Emissions of Gases and Aerosols from Nature), *Atmos. Chem. Phys.*, 6, 3181–3210, <https://doi.org/10.5194/acp-6-3181-2006>, 2006.
- Guenther, A. B., Jiang, X., Heald, C. L., Sakulyanontvittaya, T., Duhl, T., Emmons, L. K., and Wang, X.: The Model of Emissions of Gases and Aerosols from Nature version 2.1 (MEGAN2.1): an extended and updated framework for modeling biogenic emissions, *Geosci. Model Dev.*, 5, 1471–1492, <https://doi.org/10.5194/gmd-5-1471-2012>, 2012.
- Heckel, A., Kim, S.-W., Frost, G. J., Richter, A., Trainer, M., and Burrows, J. P.: Influence of low spatial resolution a priori data on tropospheric NO<sub>2</sub> satellite retrievals, *Atmos. Meas. Tech.*, 4, 1805–1820, <https://doi.org/10.5194/amt-4-1805-2011>, 2011.
- Hu, L., Jacob, D. J., Liu, X., Zhang, Y., Zhang, L., Kim, P. S., Sulprizio, M. P., and Yantosca, R. M.: Global budget of tropospheric ozone: Evaluating recent model advances with satellite (OMI), aircraft (IAGOS), and ozonesonde observations, *Atmos. Environ.*, 167, 323–334, <https://doi.org/10.1016/j.atmosenv.2017.08.036>, 2017.
- Huijnen, V., Eskes, H. J., Poupkou, A., Elbern, H., Boersma, K. F., Foret, G., Sofiev, M., Valdebenito, A., Flemming, J., Stein, O., Gross, A., Robertson, L., D’Isidoro, M., Kioutsioukis, I., Friese, E., Amstrup, B., Bergstrom, R., Strunk, A., Vira, J., Zyryanov, D., Maurizi, A., Melas, D., Peuch, V.-H., and Zerefos, C.: Comparison of OMI NO<sub>2</sub> tropospheric columns with an ensemble of global and European regional air quality models, *Atmos. Chem. Phys.*, 10, 3273–3296, <https://doi.org/10.5194/acp-10-3273-2010>, 2010.
- Im, U., Bianconi, R., Kioutsioukis, I., Badia, A., Bellasio, R., Brunner, D., Balzarini, A., Bar, R., Chemel, C., Curci, G., Flemming, J., Forkel, R., Giordano, L., Hirtl, M., Hodzic, A., Honzak, L., Jorba, O., Jim, P., Knote, C., Kuenen, J. J. P., Makar, P. A., Manders-groot, A., Pirovano, G., Pouliot, G., San, R., Neal, L., Juan, L. P., Savage, N., Schroder, W., Sokhi, R. S., Syrakov, D., Torian, A., Tuccella, P., Werhahn, J., Wolke, R., Yahya, K., Zabkar, R., Zhang, Y., Zhang, J., and Hogrefe, C.: Evaluation of operational on-line-coupled regional air quality models over Europe and North America in the context of AQMEII phase 2, Part I : Ozone, *Atmos. Environ.*, 115, 404–420, <https://doi.org/10.1016/j.atmosenv.2014.09.042>, 2015.
- Inness, A., Blechschmidt, A.-M., Bouarar, I., Chabrilat, S., Crepulja, M., Engelen, R. J., Eskes, H., Flemming, J., Gaudel, A., Hendrick, F., Huijnen, V., Jones, L., Kapsomenakis, J., Katragkou, E., Keppens, A., Langerock, B., de Mazière, M., Melas, D., Parrington, M., Peuch, V. H., Razinger, M., Richter, A., Schultz, M. G., Suttie, M., Thouret, V., Vrekoussis, M., Wagner, A., and Zerefos, C.: Data assimilation of satellite-retrieved ozone, carbon monoxide and nitrogen dioxide with ECMWF’s Composition-IFS, *Atmos. Chem. Phys.*, 15, 5275–5303, <https://doi.org/10.5194/acp-15-5275-2015>, 2015.
- IPCC: Climate Change 2013, the Physical Science Basis. Working Group I contribution to the fifth assessment report of the Intergovernmental Panel on Climate Change, Cambridge University Press, Cambridge, 2013.
- Jaeglé, L., Steinberger, L., Martin, R. V., and Chance, K.: Global partitioning of NO<sub>x</sub> sources using satellite observations: Relative roles of fossil fuel combustion, biomass burning and soil emissions, *Faraday Discuss.*, 130, 407–423, <https://doi.org/10.1039/b502128f>, 2005.
- Janssen, R. H. H., Vilà-Guerau de Arellano, J., Ganzeveld, L. N., Kabat, P., Jimenez, J. L., Farmer, D. K., van Heerwaarden, C. C., and Mammarella, I.: Combined effects of surface conditions, boundary layer dynamics and chemistry on diurnal SOA evolution, *Atmos. Chem. Phys.*, 12, 6827–6843, <https://doi.org/10.5194/acp-12-6827-2012>, 2012.
- Jin, X., Fiore, A. M., Murray, L. T., Valin, L. C., Lamsal, L. N., Duncan, B., Folkert Boersma, K., De Smedt, I., Abad, G. G., Chance, K., and Tonnesen, G. S.: Evaluating a Space-Based Indicator of Surface Ozone-NO<sub>x</sub>-VOC Sensitivity Over Midlatitude Source Regions and Application to Decadal Trends, *J. Geophys. Res.-Atmos.*, 122, 10439–10461, <https://doi.org/10.1002/2017JD026720>, 2017.
- Kavassalis, S. C. and Murphy, J. G.: Understanding ozone-meteorology correlations: A role for dry deposition, *Geophys. Res. Lett.*, 44, 2922–2931, <https://doi.org/10.1002/2016GL071791>, 2017.
- Kleipool, Q. L., Dobber, M. R., de Haan, J. F., and Levett, P. F.: Earth surface reflectance climatology from 3 years of OMI data, *J. Geophys. Res.-Atmos.*, 113, 1–22, <https://doi.org/10.1029/2008JD010290>, 2008.
- Knote, C., Tuccella, P., Curci, G., Emmons, L., Orlando, J. J., Madronich, S., Baró, R., Jiménez-Guerrero, P., Luecken, D., Hogrefe, C., Forkel, R., Werhahn, J., Hirtl, M., Pérez, J. L., San José, R., Giordano, L., Brunner, D., Yahya, K., and Zhang, Y.: Influence of the choice of gas-phase mechanism on predictions of key gaseous pollutants during the AQMEII phase-2 intercomparison, *Atmos. Environ.*, 115, 553–568, <https://doi.org/10.1016/j.atmosenv.2014.11.066>, 2015.
- Kuenen, J. J. P., Visschedijk, A. J. H., Jozwicka, M., and Denier van der Gon, H. A. C.: TNO-MACC\_II emission inventory; a multi-year (2003–2009) consistent high-resolution European emission inventory for air quality modelling, *Atmos. Chem. Phys.*, 14, 10963–10976, <https://doi.org/10.5194/acp-14-10963-2014>, 2014.
- Lamsal, L. N., Martin, R. V., van Donkelaar, A., Steinbacher, M., Celarier, E. A., Bucsela, E., Dunlea, E. J., and Pinto, J. P.: Ground-level nitrogen dioxide concentrations inferred from the satellite-borne Ozone Monitoring Instrument, *J. Geophys. Res.*, 113, D16308, <https://doi.org/10.1029/2007JD009235>, 2008.
- Lamsal, L. N., Martin, R. V., Van Donkelaar, A., Celarier, E. A., Bucsela, E. J., Boersma, K. F., Dirksen, R., Luo, C., and Wang, Y.: Indirect validation of tropospheric nitrogen dioxide retrieved from the OMI satellite instrument: Insight into the seasonal variation of nitrogen oxides at northern midlatitudes, *J. Geophys. Res.-Atmos.*, 115, 1–15, <https://doi.org/10.1029/2009JD013351>, 2010.
- Lamsal, L. N., Martin, R. V., Padmanabhan, A., van Donkelaar, A., Zhang, Q., Sioris, C. E., Chance, K., Kurosu, T. P., and Newchurch, M. J.: Application of satellite

- observations for timely updates to global anthropogenic NO<sub>x</sub> emission inventories, *Geophys. Res. Lett.*, 38, 1–5, <https://doi.org/10.1029/2010GL046476>, 2011.
- Lathière, J., Hauglustaine, D. A., De Noblet-Ducoudré, N., Krinner, G., and Folberth, G. A.: Past and future changes in biogenic volatile organic compound emissions simulated with a global dynamic vegetation model, *Geophys. Res. Lett.*, 32, 1–4, <https://doi.org/10.1029/2005GL024164>, 2005.
- Lelieveld, J., Evans, J. S., Fnais, M., Giannadaki, D., and Pozzer, A.: The contribution of outdoor air pollution sources to premature mortality on a global scale, *Nature*, 525, 367–371, <https://doi.org/10.1038/nature15371>, 2015.
- Levelt, P. F., den Oord, G. H. J., Dobber, M. R., Malkki, A., Visser, H., de Vries, J., Stammes, P., Lundell, J. O. V., and Saari, H.: The Ozone Monitoring Instrument, *IEEE T. Geosci. Remote*, 44, 1093–1101, <https://doi.org/10.1109/Tgrs.2006.872333>, 2006.
- Li, J. and Wang, Y.: Inferring the anthropogenic NO<sub>x</sub> emission trend over the United States during 2003–2017 from satellite observations: Was there a flattening of the emission trend after the Great Recession?, *Atmos. Chem. Phys. Discuss.*, <https://doi.org/10.5194/acp-2019-472>, in review, 2019.
- Li, J., Wang, Y., and Qu, H.: Dependence of Summertime Surface Ozone on NO<sub>x</sub> and VOC Emissions Over the United States: Peak Time and Value, *Geophys. Res. Lett.*, 46, 3540–3550, <https://doi.org/10.1029/2018GL081823>, 2019.
- Lorente, A., Folkert Boersma, K., Yu, H., Dörner, S., Hilboll, A., Richter, A., Liu, M., Lamsal, L. N., Barkley, M., De Smedt, I., Van Roozendaal, M., Wang, Y., Wagner, T., Beirle, S., Lin, J.-T., Krotkov, N., Stammes, P., Wang, P., Eskes, H. J., and Krol, M.: Structural uncertainty in air mass factor calculation for NO<sub>2</sub> and HCHO satellite retrievals, *Atmos. Meas. Tech.*, 10, 759–782, <https://doi.org/10.5194/amt-10-759-2017>, 2017.
- Lorente, A., Boersma, K., Eskes, H., Veeffkind, J. P., Van Geffen, J. H. G. M., De Zeeuw, M., Denier van der Gon, H., Beirle, S., and Krol, M. C.: Quantification of nitrogen oxides emissions from build-up of pollution over Paris with TROPOMI, *Sci. Rep.*, in review, 2019.
- Maasakkers, J. D.: Vital improvements to the retrieval of tropospheric NO<sub>2</sub> columns from the Ozone Monitoring Instrument (MSc thesis), Eindhoven (NL), available at: [https://kfolkertboersma.files.wordpress.com/2017/10/maasakkers\\_msc\\_2013.pdf](https://kfolkertboersma.files.wordpress.com/2017/10/maasakkers_msc_2013.pdf) (last access: 18 February 2019), 2013.
- Mar, K. A., Ojha, N., Pozzer, A., and Butler, T. M.: Ozone air quality simulations with WRF-Chem (v3.5.1) over Europe: model evaluation and chemical mechanism comparison, *Geosci. Model Dev.*, 9, 3699–3728, <https://doi.org/10.5194/gmd-9-3699-2016>, 2016.
- Marécal, V., Peuch, V.-H., Andersson, C., Andersson, S., Arteta, J., Beekmann, M., Benedictow, A., Bergström, R., Bessagnet, B., Cansado, A., Chéroux, F., Colette, A., Coman, A., Curier, R. L., Denier van der Gon, H. A. C., Drouin, A., Elbern, H., Emili, E., Engelen, R. J., Eskes, H. J., Foret, G., Friese, E., Gauss, M., Giannaros, C., Guth, J., Joly, M., Jaumouillé, E., Josse, B., Kadyrov, N., Kaiser, J. W., Krajsek, K., Kuenen, J., Kumar, U., Liora, N., Lopez, E., Malherbe, L., Martinez, I., Melas, D., Meleux, F., Menut, L., Moinat, P., Morales, T., Parmentier, J., Piacentini, A., Plu, M., Poupkou, A., Queguiner, S., Robertson, L., Rouil, L., Schaap, M., Segers, A., Sofiev, M., Tarasson, L., Thomas, M., Timmermans, R., Valdebenito, Á., van Velthoven, P., van Versendaal, R., Vira, J., and Ung, A.: A regional air quality forecasting system over Europe: the MACC-II daily ensemble production, *Geosci. Model Dev.*, 8, 2777–2813, <https://doi.org/10.5194/gmd-8-2777-2015>, 2015.
- Martin, R., Jacob, D., Chance, K., Kurosu, T. P., Palmer, P. I., and Evans, M. J.: Global inventory of nitrogen oxide emissions constrained by space-based observations of NO<sub>2</sub> columns, *J. Geophys. Res.*, 108, 1–12, <https://doi.org/10.1029/2003JD003453>, 2003.
- Millán, M. M., Salvador, R., Mantilla, E., and Kallos, G.: Photooxidant dynamics in the Mediterranean basin in summer: Results from European research projects, *J. Geophys. Res.-Atmos.*, 102, 8811–8823, <https://doi.org/10.1029/96JD03610>, 1997.
- Miyazaki, K., Eskes, H. J., Sudo, K., and Zhang, C.: Global lightning NO<sub>x</sub> production estimated by an assimilation of multiple satellite data sets, *Atmos. Chem. Phys.*, 14, 3277–3305, <https://doi.org/10.5194/acp-14-3277-2014>, 2014.
- Miyazaki, K., Eskes, H., Sudo, K., Boersma, K. F., Bowman, K., and Kanaya, Y.: Decadal changes in global surface NO<sub>x</sub> emissions from multi-constituent satellite data assimilation, *Atmos. Chem. Phys.*, 17, 807–837, <https://doi.org/10.5194/acp-17-807-2017>, 2017.
- Oikawa, P. Y., Ge, C., Wang, J., Eberwein, J. R., Liang, L. L., Allsman, L. A., Grantz, D. A., and Jenerette, G. D.: Unusually high soil nitrogen oxide emissions influence air quality in a high-temperature agricultural region, *Nat. Commun.*, 6, 8753, <https://doi.org/10.1038/ncomms9753>, 2015.
- Ott, L. E., Pickering, K. E., Stenichikov, G. L., Allen, D. J., DeCaria, A. J., Ridley, B., Lin, R.-F., Lang, S., and Tao, W.-K.: Production of lightning NO<sub>x</sub> and its vertical distribution calculated from three-dimensional cloud-scale chemical transport model simulations, *J. Geophys. Res.*, 115, D04301, <https://doi.org/10.1029/2009JD011880>, 2010.
- Pickering, K. E., Bucsel, E., Allen, D., Ring, A., Holzworth, R., and Krotkov, N.: Estimates of lightning NO<sub>x</sub> production based on OMI NO<sub>2</sub> observations over the Gulf of Mexico, *J. Geophys. Res.*, 121, 8668–8691, <https://doi.org/10.1002/2015JD024179>, 2016.
- Pope, R. J., Chipperfield, M. P., Savage, N. H., Ordóñez, C., Neal, L. S., Lee, L. A., Dhomse, S. S., Richards, N. A. D., and Keskula, T. D.: Evaluation of a regional air quality model using satellite column NO<sub>2</sub>: treatment of observation errors and model boundary conditions and emissions, *Atmos. Chem. Phys.*, 15, 5611–5626, <https://doi.org/10.5194/acp-15-5611-2015>, 2015.
- Pouliot, G., Denier van der Gon, H. A., Kuenen, J., Zhang, J., Moran, M. D., and Makar, P. A.: Analysis of the emission inventories and model-ready emission datasets of Europe and North America for phase 2 of the AQMEII project, *Atmos. Environ.*, 115, 345–360, <https://doi.org/10.1016/j.atmosenv.2014.10.061>, 2015.
- Price, C. and Rind, D.: What determines the cloud-to-ground lightning fraction in thunderstorms?, *Geophys. Res. Lett.*, 20, 463–466, <https://doi.org/10.1029/93GL00226>, 1993.
- Pusede, S. E., Steiner, A. L., and Cohen, R. C.: Temperature and Recent Trends in the Chemistry of Continental Surface Ozone, *Chem. Rev.*, 115, 3898–3918, <https://doi.org/10.1021/cr5006815>, 2015.

- Querol, X., Gangoiti, G., Mantilla, E., Alastuey, A., Minguillón, M. C., Amato, F., Reche, C., Viana, M., Moreno, T., Karanasiou, A., Rivas, I., Pérez, N., Ripoll, A., Brines, M., Ealo, M., Pandolfi, M., Lee, H.-K., Eun, H.-R., Park, Y.-H., Escudero, M., Beddows, D., Harrison, R. M., Bertrand, A., Marchand, N., Lyasota, A., Codina, B., Olid, M., Udina, M., Jiménez-Esteve, B., Soler, M. R., Alonso, L., Millán, M., and Ahn, K.-H.: Phenomenology of high-ozone episodes in NE Spain, *Atmos. Chem. Phys.*, 17, 2817–2838, <https://doi.org/10.5194/acp-17-2817-2017>, 2017.
- Rasool, Q. Z., Zhang, R., Lash, B., Cohan, D. S., Cooter, E. J., Bash, J. O., and Lamsal, L. N.: Enhanced representation of soil NO emissions in the Community Multiscale Air Quality (CMAQ) model version 5.0.2, *Geosci. Model Dev.*, 9, 3177–3197, <https://doi.org/10.5194/gmd-9-3177-2016>, 2016.
- Rasool, Q. Z., Bash, J. O., and Cohan, D. S.: Mechanistic representation of soil nitrogen emissions in the Community Multiscale Air Quality (CMAQ) model v 5.1, *Geosci. Model Dev.*, 12, 849–878, <https://doi.org/10.5194/gmd-12-849-2019>, 2019.
- Rouïl, L. and Meleux, F.: Annual Air Quality Assessment Report 2015, Tech. rep., Copernicus Atmospheric Monitoring Service, available at: [https://policy.atmosphere.copernicus.eu/reports/CAMS-71\\_SC22016\\_D71.1.3\\_201801\\_V2.pdf](https://policy.atmosphere.copernicus.eu/reports/CAMS-71_SC22016_D71.1.3_201801_V2.pdf) (last access: 17 January 2019), 2018.
- Russell, A. R., Perring, A. E., Valin, L. C., Bucsel, E. J., Browne, E. C., Wooldridge, P. J., and Cohen, R. C.: A high spatial resolution retrieval of NO<sub>2</sub> column densities from OMI: method and evaluation, *Atmos. Chem. Phys.*, 11, 8543–8554, <https://doi.org/10.5194/acp-11-8543-2011>, 2011.
- Schaap, M., Cuvelier, C., Hendriks, C., Bessagnet, B., Baldasano, J., Colette, A., Thunis, P., Karam, D., Fagerli, H., Graff, A., Kranenburg, R., Nyiri, A., Pay, M., Rouïl, L., Schulz, M., Simpson, D., Stern, R., Terrenoire, E., and Wind, P.: Performance of European chemistry transport models as function of horizontal resolution, *Atmos. Environ.*, 112, 90–105, <https://doi.org/10.1016/j.atmosenv.2015.04.003>, 2015.
- Sillman, S., Logan, J., and Wofsy, S.: The sensitivity of ozone to nitrogen oxides and hydrocarbons in regional ozone episodes, *J. Geophys. Res.*, 95, 1837–1851, <https://doi.org/10.1029/JD095iD02p01837>, 1990.
- Sitch, S., Cox, P. M., Collins, W. J., and Huntingford, C.: Indirect radiative forcing of climate change through ozone effects on the land-carbon sink, *Nature*, 448, 791–794, <https://doi.org/10.1038/nature06059>, 2007.
- Solazzo, E., Bianconi, R., Vautard, R., Appel, K. W., Moran, M., Hogrefe, C., Bessagnet, B., Brandt, J., Christensen, J. H., Chemel, C., Coll, I., Denier van der Gon, H., Ferreira, J., Forkel, R., Francis, X. V., Grell, G., Grossi, P., Hansen, A. B., Jeričević, A., Kraljević, L., Miranda, A. I., Nopmongkol, U., Pirovano, G., Prank, M., Riccio, A., Sartelet, K. N., Schaap, M., Silver, J. D., Sokhi, R. S., Vira, J., Werhahn, J., Wolke, R., Yarwood, G., Zhang, J., Rao, T. S., and Galmarini, S.: Model evaluation and ensemble modelling of surface-level ozone in Europe and North America in the context of AQMEII, *Atmos. Environ.*, 53, 60–74, <https://doi.org/10.1016/j.atmosenv.2012.01.003>, 2012.
- Stavrakou, T., Müller, J.-F., Boersma, K. F., van der A, R. J., Kurokawa, J., Ohara, T., and Zhang, Q.: Key chemical NO<sub>x</sub> sink uncertainties and how they influence top-down emissions of nitrogen oxides, *Atmos. Chem. Phys.*, 13, 9057–9082, <https://doi.org/10.5194/acp-13-9057-2013>, 2013.
- Steinbacher, M., Zellweger, C., Schwarzenbach, B., Bugmann, S., Buchmann, B., Ordóñez, C., Prevot, A. S., and Hueglin, C.: Nitrogen oxide measurements at rural sites in Switzerland: Bias of conventional measurement techniques, *J. Geophys. Res.-Atmos.*, 112, 1–13, <https://doi.org/10.1029/2006JD007971>, 2007.
- Steinkamp, J. and Lawrence, M. G.: Improvement and evaluation of simulated global biogenic soil NO emissions in an AC-GCM, *Atmos. Chem. Phys.*, 11, 6063–6082, <https://doi.org/10.5194/acp-11-6063-2011>, 2011.
- Stohl, A., Williams, E., Wotawa, G., and Kromp-Kolb, H.: A European inventory of soil nitric oxide emissions and the effect of these emissions on the photochemical formation of ozone, *Atmos. Environ.*, 30, 3741–3755, [https://doi.org/10.1016/1352-2310\(96\)00104-5](https://doi.org/10.1016/1352-2310(96)00104-5), 1996.
- Tawfik, A. B. and Steiner, A. L.: A proposed physical mechanism for ozone-meteorology correlations using land-atmosphere coupling regimes, *Atmos. Environ.*, 72, 50–59, <https://doi.org/10.1016/j.atmosenv.2013.03.002>, 2013.
- Terrenoire, E., Bessagnet, B., Rouïl, L., Tognet, F., Pirovano, G., Létinois, L., Beauchamp, M., Colette, A., Thunis, P., Amann, M., and Menut, L.: High-resolution air quality simulation over Europe with the chemistry transport model CHIMERE, *Geosci. Model Dev.*, 8, 21–42, <https://doi.org/10.5194/gmd-8-21-2015>, 2015.
- Tuccella, P., Curci, G., Visconti, G., Bessagnet, B., Menut, L., and Park, R. J.: Modeling of gas and aerosol with WRF/Chem over Europe: Evaluation and sensitivity study, *J. Geophys. Res.-Atmos.*, 117, 1–15, <https://doi.org/10.1029/2011JD016302>, 2012.
- Valin, L. C., Russell, A. R., Hudman, R. C., and Cohen, R. C.: Effects of model resolution on the interpretation of satellite NO<sub>2</sub> observations, *Atmos. Chem. Phys.*, 11, 11647–11655, <https://doi.org/10.5194/acp-11-11647-2011>, 2011.
- Veefkind, J. P., Aben, I., McMullan, K., Förster, H., de Vries, J., Otter, G., Claas, J., Eskes, H. J., de Haan, J. F., Kleipool, Q., van Weele, M., Hasekamp, O., Hoogeveen, R., Landgraf, J., Snel, R., Tol, P., Ingmann, P., Voors, R., Kruizinga, B., Vink, R., Visser, H., and Levelt, P. F.: TROPOMI on the ESA Sentinel-5 Precursor: A GMES mission for global observations of the atmospheric composition for climate, air quality and ozone layer applications, *Remote Sens. Environ.*, 120, 70–83, <https://doi.org/10.1016/j.rse.2011.09.027>, 2012.
- Veefkind, J. P., de Haan, J. F., Sneep, M., and Levelt, P. F.: Improvements to the OMI O<sub>2</sub>–O<sub>2</sub> operational cloud algorithm and comparisons with ground-based radar–lidar observations, *Atmos. Meas. Tech.*, 9, 6035–6049, <https://doi.org/10.5194/amt-9-6035-2016>, 2016.
- Verstraeten, W. W., Neu, J. L., Williams, J. E., Bowman, K. W., Worden, J. R., and Boersma, K. F.: Rapid increases in tropospheric ozone production and export from China, *Nat. Geosci.*, 8, 690–695, <https://doi.org/10.1038/ngeo2493>, 2015.
- Vinken, G. C. M., Boersma, K. F., Maasakkers, J. D., Adon, M., and Martin, R. V.: Worldwide biogenic soil NO<sub>x</sub> emissions inferred from OMI NO<sub>2</sub> observations, *Atmos. Chem. Phys.*, 14, 10363–10381, <https://doi.org/10.5194/acp-14-10363-2014>, 2014a.
- Vinken, G. C. M., Boersma, K. F., van Donkelaar, A., and Zhang, L.: Constraints on ship NO<sub>x</sub> emissions in Europe using GEOS-Chem and OMI satellite NO<sub>2</sub> observations, *Atmos.*

- Chem. Phys., 14, 1353–1369, <https://doi.org/10.5194/acp-14-1353-2014>, 2014b.
- Williams, J. E., Boersma, K. F., Le Sager, P., and Verstraeten, W. W.: The high-resolution version of TM5-MP for optimized satellite retrievals: description and validation, *Geosci. Model Dev.*, 10, 721–750, <https://doi.org/10.5194/gmd-10-721-2017>, 2017.
- Willmott, C.: Some comments on the evaluation of model performance, *B. Am. Meteor. Soc.*, 63, 1309–1313, [https://doi.org/10.1175/1520-0477\(1982\)063<1309:SCOTEO>2.0.CO;2](https://doi.org/10.1175/1520-0477(1982)063<1309:SCOTEO>2.0.CO;2), 1982.
- Wong, J., Barth, M. C., and Noone, D.: Evaluating a lightning parameterization based on cloud-top height for mesoscale numerical model simulations, *Geosci. Model Dev.*, 6, 429–443, <https://doi.org/10.5194/gmd-6-429-2013>, 2013.
- Zara, M., Boersma, K. F., De Smedt, I., Richter, A., Peters, E., van Geffen, J. H. G. M., Beirle, S., Wagner, T., Van Roozendaal, M., Marchenko, S., Lamsal, L. N., and Eskes, H. J.: Improved slant column density retrieval of nitrogen dioxide and formaldehyde for OMI and GOME-2A from QA4ECV: intercomparison, uncertainty characterisation, and trends, *Atmos. Meas. Tech.*, 11, 4033–4058, <https://doi.org/10.5194/amt-11-4033-2018>, 2018.
- Zaveri, R. and Peters, L.: A new lumped structure photochemical mechanism for large-scale applications, *J. Geophys. Res.-Atmos.*, 104, 30387–30415, <https://doi.org/10.1029/1999JD900876>, 1999.
- Zhou, Y., Brunner, D., Hueglin, C., Henne, S., and Staehelin, J.: Changes in OMI tropospheric NO<sub>2</sub> columns over Europe from 2004 to 2009 and the influence of meteorological variability, *Atmos. Environ.*, 46, 482–495, <https://doi.org/10.1016/j.atmosenv.2011.09.024>, 2012.